Modeling and Numerical Investigation of Mechanical Twinning in β-HMX Crystals Subjected to Shock Loading

Xiaoyu Zhang* and Caglar Oskay†

Department of Civil and Environmental Engineering
Vanderbilt University
Nashville, TN 37212

Abstract

This manuscript establishes a Crystal Plasticity Finite Element (CPFE) model with large volumetric deformation for β-HMX (1,3,5,7-tetranitro-1,3,5,7-tetrazocane) energetic crystals with emphasis on the deformation twinning behavior under shock loading conditions. The CPFE model captures the nonlinear response of the monoclinic crystal through the application of large volumetric change under shock condition, dislocation slip at low and high moving speeds and mechanical twinning idealized by the twin volume fraction evolution. The twinning behavior is distinguished from dislocation slip through the decomposition of the plastic velocity gradient in which dislocation slip, twinning and slip in the twinned region are separately considered. Third-order Birch Murnaghan EOS is incorporated in the CPFE framework to describe the volumetric deformation under extreme pressure induced by explosion or impact. The results of the numerical investigations show that the twinning behavior exhibits strong orientation dependency, which becomes more evident at higher loading regime. Particle shape significantly affects the twin concentration. Peak twin volume fraction in HMX polycrystalline with regularized particle shapes is lower compared with mesostructure with realistic particle morphologies.

Keywords: Energetic materials, Crystal plasticity, Dynamic behavior, Polycrystalline materials, Twinning.

*Author address: VU Station B#351831, 2301 Vanderbilt Place, Nashville, TN 37235. Email: xiaoyu.zhang@vanderbilt.edu

†Corresponding author address: VU Station B#351831, 2301 Vanderbilt Place, Nashville, TN 37235. Email: caglar.oskay@vanderbilt.edu

1 Introduction

HMX (1,3,5,7-tetranitro-1,3,5,7-tetrazocane) is an energetic molecular crystal with numerous potential deformation mechanisms (dislocation slip, mechanical twinning, adiabatic shear, interacting thermo-plastic processes within the microstructure [18, 32, 59, 68, 73, 78, 84]). Among these, deformation twinning has been regarded as an important deformation mechanism as evidenced by experiments [23, 56, 63] and molecular dynamics simulations [2, 76] at static and high rate regimes. However, the available crystal plasticity models [5, 7, 25, 28, 75, 82] either focus on describing high rate deformation in HMX using dislocation slip alone, or take the twinning system as an additional slip system idealized using similar flow and hardening evolution laws as those for slip. In view of the potential importance of twinning in describing the mechanical response of HMX, this manuscript investigates the twinning deformation within HMX single crystals and polycrystal mesostructures at various orientations and loading rates.

Mechanical twinning in HMX and HMX-based composites has been identified as a dominant deformation mechanism in compression tests [1, 23, 45, 56, 63, 68]. Twinning also affects the deformation phenomena at gas gun strain rates [44, 82], although fewer experimental data are available at high strain rates. Cady [12] observed that β-polymorph of HMX shows growth twinning on (101) plane ($P2_1/n$ space group), and also exhibits deformation twinning on the same plane. Palmer and Field [56] identified that, under compressive loading, a shear stress parallel to (101) changes the orientation of the lattice and leads to the formation of the twin band. Gallagher et al. [23] observed that the primary twin with the twinning elements $K_1 : (101)$, $\eta_1 : [10\bar{1}]$, $K_2 : (001)$, $\eta_2 : [100]$, and the twinning shear strain was calculated to be 0.353. Since K_1, η_1, K_2 and η_2 are all rational, such a twin is a compound twin [10]. Elastic twinning [14, 40] has also been observed in the tension/compression tests of HMX performed by Palmer and Field [56]. Cady [12] also reported the temperature dependence of elastic twinning behavior for HMX. However, Gallagher et al. [23] observed that this recovery behavior took 30 minutes for the specimen to fully recover, which makes its contribution more relevant to the static or quasi-static cases compared to impact/shock conditions. Efforts are also put on the numerical investigation of twinning at the molecular scale. Armstrong et al. [2] proposed a two-step process for the deformation twinning (twinning elements $K_1 : (101)$, $\eta_1 : [10\bar{1}]$, $K_2 : (10\bar{1})$, $\eta_2 : [101]$) in which the twinning orientation relationship was visualized to occur by a rotation of 180° about the twinning η_1 direction, followed by a parallel translation. Despite the difference of conjugate twinning plane K_2 and conjugate twinning direction η_2 in [2, 23], both of them identified the twinning system to be $(101)[10\bar{1}]$. Wen et al. [76] revealed the twin induced enhancement of shock sensitivity by comparing the response of perfect HMX and twinned HMX. Khan et al. [39] observed that twinning significantly affects the behavior of $(101)[10\bar{1}]$ screw dislocations by making the asymmetric dislocation behavior more symmetric.

In this manuscript, we model and simulate the dynamic behavior of β-HMX crystals with

emphasis on twinning phenomenon under different loading rates. Twin model of the monoclinic crystal is developed in a CPFE framework proposed by Becker [8] to capture dynamic responses up to shock loading regime. In this CPFE formulation with large volumetric deformation, the third order Birch Murnaghan (BM) Equation-Of-State (EOS) [11] is employed to describe the pressure-volume relationship, and the Gruneisen tensor is incorporated to characterize the coupling between pressure and distortion for this monoclinic crystal. To capture the orientation dependent deformation ([20, 51, 80]) in β-HMX under dynamic loads, the elastic model of HMX not only incorporates the EOS, but also integrates the pressure dependency in the thirteen elasticity coefficients of the monoclinic crystal. Dislocation slip within β-HMX twinned/untwinned crystals subjected to dynamic loads are depicted by the evolution law proposed by Zhang and Oskay [85] in which both thermal activation and phonon drag mechanisms are considered such that both slow dislocation motion (1e-6 m/s - 1 m/s) and faster dislocation motion (>1 m/s) can be captured. The proposed CPFE model is employed to investigate twin accumulation in single and polycrystal HMX configurations. The study of twin concentration within HMX polycrystalline specimens is focused on the effect of particle geometry and crystal misorientation. In this study, mechanical twinning in HMX crystal is incorporated as an independent physical phenomenon, and twinning evolution in single crystalline and polycrystalline β-HMX at high strain rates is investigated.

The remainder of this manuscript is structured as follows: Section 2 provides the crystal plasticity constitutive relations employed in the simulation of the dynamic response of β-HMX at the mesoscale, as well as the detailed twinning evolution equations. Section 3 describes the parameter calibration, including the parameters of thermo elastic deformation, dislocation slip and mechanical twinning. Numerical investigations that utilize the aforementioned CPFE framework and embedded twinning model to predict twin concentrations in both single crystal and polycrystalline configurations are discussed in Section 4. Section 5 provides the summary and conclusions.

2 Constitutive Model of β-HMX

The anisotropic deformation behavior of HMX at the crystal scale is modeled using the Crystal Plasticity Finite Element (CPFE) model accounting for the large volume change under shock loading, dislocation slip and mechanical twinning.

2.1 Kinematics

The model kinematics is based on multiplicative decomposition of the deformation gradient and the assumption that deviatoric thermo-elastic stretch remains small relative to volumetric deformation [6]. The deformation gradient $\boldsymbol{F}$ is decomposed as

$$\boldsymbol{F} = \boldsymbol{V}^e \cdot \boldsymbol{R}^e \cdot \boldsymbol{F}^p \tag{1}$$

where $\boldsymbol{V}^e$ is the left stretch tensor representing the elastic stretch of the lattice, $\boldsymbol{R}^e$ is the orthogonal tensor defining the rotation and reorientation of the material point in a grain, and $\boldsymbol{F}^p$ represents the plastic deformation induced by dislocation slip and twinning evolution in the crystallographic slip/twin systems.

The above decomposition introduces two intermediate configurations, stress-free intermediate configuration (after $\boldsymbol{F}^p$) and the rotated stress-free intermediate configuration (after $\boldsymbol{R}^e \cdot \boldsymbol{F}^p$). Plasticity update is performed in the former configuration. All quantities with overbar in this formulation indicate representation in the stress-free intermediate configuration.

To characterize the elastic deformation, a logarithmic form is used for the lattice strain measure expressed in the intermediate configuration defined by $\boldsymbol{R}^e$.

$$\overline{\boldsymbol{E}} = \ln(\overline{\boldsymbol{V}}^e) \quad \text{where} \quad \overline{\boldsymbol{V}}^e = \boldsymbol{R}^{eT} \cdot \boldsymbol{V}^e \cdot \boldsymbol{R}^e \tag{2}$$

where $\overline{\boldsymbol{V}}^e$ is the right stretch tensor. It is important to note that the hydrostatic elastic strain induced by shock compression remains large despite the small deviatoric elastic strain assumption. Let $a = (\det(\boldsymbol{V}^e))^{\frac{1}{3}}$ such that $\boldsymbol{V}^e = a\boldsymbol{V}^{e\star}$ and $\det(\boldsymbol{V}^{e\star}) = 1$. Then we assume $\boldsymbol{V}^{e\star} = \boldsymbol{I} + \boldsymbol{\epsilon}^\star$, which results in

$$\boldsymbol{V}^e = a(\boldsymbol{I} + \boldsymbol{\epsilon}^\star) \tag{3}$$

where, $\boldsymbol{I}$ is the second order unit tensor, $\boldsymbol{\epsilon}^\star$ denotes the small elastic deviatoric strain tensor ($\boldsymbol{\epsilon}^\star << \boldsymbol{I}$) and $\boldsymbol{\epsilon}^\star = \boldsymbol{\epsilon}^{\star\prime} = \frac{1}{a}\boldsymbol{V}^{e\prime}$. The volumetric and deviatoric parts of $\overline{\boldsymbol{E}}$ are expressed respectively as:

$$\overline{E}_V = \overline{\boldsymbol{E}} : \boldsymbol{I} = \ln(a^3) \quad \text{and} \quad \overline{\boldsymbol{E}}' \approx \frac{1}{a}\overline{\boldsymbol{V}}^{e\prime} \tag{4}$$

After some algebra detailed in [6], the following simplified kinematics equations for small deviatoric elastic strain are obtained. The deformation rate $\boldsymbol{D}$ is described in terms of its deviatoric and volumetric components.

$$\boldsymbol{R}^{eT} \cdot \boldsymbol{D}' \cdot \boldsymbol{R}^e = \frac{1}{a}\dot{\overline{\boldsymbol{V}}}^{e\prime} + \overline{\boldsymbol{D}}' \tag{5a}$$

$$\frac{d}{dt}\big(\det(\boldsymbol{V}^e)\big) = \det(\boldsymbol{V}^e)\mathrm{tr}(\boldsymbol{D} - \overline{\boldsymbol{D}}) \tag{5b}$$

The spin tensor $\boldsymbol{W}$ is expressed as:

$$\boldsymbol{R}^{eT} \cdot \boldsymbol{W} \cdot \boldsymbol{R}^e = \boldsymbol{R}^{eT} \cdot \boldsymbol{W}^R \cdot \boldsymbol{R}^e + \overline{\boldsymbol{W}} + \frac{1}{a}[\overline{\boldsymbol{V}}^{e\prime} \cdot (\overline{\boldsymbol{D}}' + \frac{1}{2a}\dot{\overline{\boldsymbol{V}}}^{e\prime}) - (\overline{\boldsymbol{D}}' + \frac{1}{2a}\dot{\overline{\boldsymbol{V}}}^{e\prime}) \cdot \overline{\boldsymbol{V}}^{e\prime}] \tag{6}$$

where $\boldsymbol{W}^R = \dot{\boldsymbol{R}}^e \cdot \boldsymbol{R}^{eT}$, $\overline{\boldsymbol{W}}$ is the spin tensor in the stress-free intermediate configuration, $\boldsymbol{D}'$ is the deviatoric component of deformation rate, and $\overline{\boldsymbol{D}}'$ is the deviatoric component of $\overline{\boldsymbol{D}}$. The term $\overline{\boldsymbol{D}}$ is equal to $\boldsymbol{R}^{eT} \cdot \widehat{\boldsymbol{D}} \cdot \boldsymbol{R}^e$, where $\widehat{\boldsymbol{D}}$ is the symmetric part of $\widehat{\boldsymbol{L}}$ which is defined by the rotation tensor and plastic velocity gradient [6]. Eq. 5a, Eq. 5b and Eq. 6 constitute the simplified kinematics that employ small deviatoric elastic strains. These three equations are

used to respectively update the deviatoric strain, volumetric strain and rotations.

2.2 Anisotropic elasticity

At large pressures encountered in high rate conditions, the crystals undergo large volumetric deformations, and the elastic moduli are pressure dependent. The current model employs the anisotropic elasticity formulation proposed by Becker [8]. The pressure-volume relationship is described by the equation of state, and the coupling of stress and energy is captured through the Gruneisen parameter.

We employ the stress measure Becker [8] $\overline{\boldsymbol{\tau}} = J\overline{\boldsymbol{\sigma}}$ as the approximation of the conjugate stress to the logarithmic strain $\overline{\boldsymbol{E}}$ [27, 30], where $J = a^3$ is the Jacobian of the deformation gradient, and $\overline{\boldsymbol{\sigma}} = \boldsymbol{R}^{eT} \cdot \boldsymbol{\sigma} \cdot \boldsymbol{R}^{e}$. The elastic model [8] is expressed as $\overline{\boldsymbol{\tau}} = J\overline{\boldsymbol{\sigma}} = J\big[\overline{\mathbb{C}}^e : \overline{\boldsymbol{E}} + \frac{1}{2}(\overline{\boldsymbol{E}} : \frac{d\overline{\mathbb{C}}^e}{dp_{\overline{\boldsymbol{\tau}}}} : \overline{\boldsymbol{E}})\frac{dp_{\overline{\boldsymbol{\tau}}}}{d\overline{E}_V}\boldsymbol{I}\big]$, where $\overline{\mathbb{C}}^e$ is the pressure dependent elastic moduli tensor in the intermediate frame, and $p_{\overline{\boldsymbol{\tau}}}$ is pressure. The stress measure is decomposed to the deviatoric and volumetric parts with the introduction of the Gruneisen tensor and the EOS [8]:

$$\overline{\boldsymbol{\tau}}' = J\overline{\boldsymbol{\sigma}}' = J\Big[\mathbb{P}_d : \overline{\mathbb{C}}^e : \overline{\boldsymbol{E}}' + \frac{1}{3}(\mathbb{P}_d : \overline{\mathbb{C}}^e : \boldsymbol{I})\overline{E}_V - \boldsymbol{\Gamma}' e\Big] \tag{7}$$

$$\begin{aligned} p_{\overline{\boldsymbol{\tau}}} &= -J\overline{\sigma}_h \\ &= -J\Big\{\sigma_h|_{\text{EOS}} + \frac{1}{3}(\overline{\boldsymbol{E}}' : \overline{\mathbb{C}}^e : \boldsymbol{I}) + \Big[\frac{1}{2}(\overline{\boldsymbol{E}}' : \frac{d\overline{\mathbb{C}}^e}{dp_{\overline{\boldsymbol{\tau}}}} : \overline{\boldsymbol{E}}') + \frac{1}{3}(\overline{\boldsymbol{E}}' : \frac{d\overline{\mathbb{C}}^e}{dp_{\overline{\boldsymbol{\tau}}}} : \boldsymbol{I})\overline{E}_V\Big]\frac{dp_{\overline{\boldsymbol{\tau}}}}{d\overline{E}_V} - \Gamma e\Big\} \end{aligned} \tag{8}$$

where $\mathbb{P}_d$ represents a fourth order operator that extracts the deviatoric part of a second order tensor, i.e., $\mathbb{P}_d = \mathbb{I} - \frac{1}{3}\boldsymbol{I} \otimes \boldsymbol{I}$ with fourth order identity tensor, $\mathbb{I}$. e is the volumetric part of the internal energy density. $\boldsymbol{\Gamma}'$ is the deviatoric part of the Gruneisen tensor expressed as a function of the thermal expansion tensor for the anisotropic material [38]. Γ is the volumetric component of the Gruneisen tensor. The matrix form of the Gruneisen tensor [38] is given as:

$$\begin{bmatrix} \Gamma_{11} \\ \Gamma_{22} \\ \Gamma_{33} \\ \Gamma_{23} \\ \Gamma_{13} \\ \Gamma_{12} \end{bmatrix} = \frac{1}{\rho C_V} \begin{bmatrix} C_{11} & C_{12} & C_{13} & 0 & C_{15} & 0 \\ C_{12} & C_{22} & C_{23} & 0 & C_{25} & 0 \\ C_{13} & C_{23} & C_{33} & 0 & C_{35} & 0 \\ 0 & 0 & 0 & C_{44} & 0 & C_{46} \\ C_{15} & C_{25} & C_{35} & 0 & C_{55} & 0 \\ 0 & 0 & 0 & C_{46} & 0 & C_{66} \end{bmatrix} \begin{bmatrix} \alpha_{11} \\ \alpha_{22} \\ \alpha_{33} \\ \alpha_{23} \\ \alpha_{13} \\ \alpha_{12} \end{bmatrix} \tag{9}$$

where ρ is the mass density, C_V the specific heat, and α_{ij} is a component of thermal expansion tensor, $\boldsymbol{\alpha}$. Values of the thermal expansion tensor components for monoclinic β-HMX crystal were measured and provided in [19].

The part of Eq. 8 that deals with the pressure-volume relationship is replaced by an equation of state, $\sigma_h|_{\text{EOSs}}$. Various EOS have been proposed in modeling the hydrodynamic behavior of β-HMX subjected to levels of pressure induced by explosion or impact. Olinger et al.

[53] measured room temperature isotherm for β-HMX and fit the isotherm to an EOS with two fitting parameters. Yoo and Cynn [79] obtained the pressure-volume relationship of β-HMX by fitting the isotherms of unreacted HMX (with pressure up to 27 GPa and 12 GPa, respectively) to the third-order Birch Murnaghan (BM) EOS for both hydrostatic and non-hydrostatic conditions. Menikoff and Sewell [50] re-analyzed the experiments from Olinger et al. [53] and Yoo and Cynn [79] to determine which fitting form is most consistent with other data for HMX and HMX-based plastic-bonded explosives. In order to investigate the sensitivity of bulk modulus of β-HMX to the choice of EOS and weight scheme, Sewell et al. [66] applied three forms of EOS [50, 53, 79] to isotherms for β-HMX obtained from their simulations and two additional simulations from [69], and they concluded that the third-order BM EOS, fit with a weighting scheme that emphasizes low-pressure data, and consistently yields initial moduli in closest agreement with values obtained from theoretical predictions. Gump and Peiris [26] obtained the pressure-volume third-order BM EOS of β-HMX at temperatures of 30 °C, 100 °C, and 140 °C under both hydrostatic and non-hydrostatic compressions up to 5.8 GPa and 4 GPa, and observed phase transition from β to δ beyond these pressures. In contrast, Hooks et al. [31] did not observe phase transition in the isentropic compression reverberation experiments performed on (010) and (011) oriented HMX crystals up to a peak stress of about 54 GPa.

Despite the controversy on the pressures to phase transition, References [16, 43, 58] employed data from both [79] and [26] to fit third-order BM EOS for β-HMX with pressure up to 12 GPa. Under larger pressure, additional physico-chemical mechanisms such as chemical reactions and crystal melting are involved in the deformation process. Austin et al. [5] described the thermo-elasto-viscoplastic behavior of the β phase HMX by incorporating a Murnaghan EOS into the crystal plasticity model, in which decomposition reaction and crystal melting are considered to reproduce Hugoniot data [47] with pressure larger than 40 GPa. Recently, White and Tarver [77] developed the parameters of Jones-Wilkins-Lee (JWL) EOS for HMX single crystal with mass density 1.905 g/cm^3 and of JWL EOS for reaction products.

Following Refs [16, 43, 58], third order BM EOS is employed in this study:

$$\sigma_h|_{\text{EOS}} = -\frac{3B_0}{2}\Big(J^{-\frac{7}{3}} - J^{-\frac{5}{3}}\Big)\Big[1 + \frac{3}{4}(B_0' - 4)\Big(J^{-\frac{2}{3}} - 1\Big)\Big] \tag{10}$$

where B_0 is the bulk modulus at zero pressure, and B_0' is the derivative of the bulk modulus with respect to pressure at zero pressure. The volumetric part of the internal energy density e is then expressed as

$$e = \frac{9B_0}{16}J^{-1}\Big[\Big(J^{-\frac{2}{3}} - 1\Big)^3 B_0' + \Big(J^{-\frac{2}{3}} - 1\Big)^2\Big(6 - 4J^{-\frac{2}{3}}\Big)\Big] \tag{11}$$

The internal energy density contribution due to plastic dissipation is relatively small at the high strain rates considered in this manuscript and therefore not included.

2.3 Mechanical twinning model

In this study, the twinning relation proposed by Kalidindi [36] is employed to capture the twinning phenomenon in HMX crystal. While twinning models for a variety of materials have been developed and employed, twinning modeling work for β-HMX crystal is relatively scarce. Zamiri and De [81] modeled twinning on the $(101)[10\bar{1}]$ as an additional slip system idealized using the same flow and hardening evolution laws as for slip. Zecevic et al. [83] investigated twin model in single crystal configuration with focus on the relationship between the behavior for twinning and crystal orientation.

The velocity gradient in the stress-free intermediate configuration, $\overline{\boldsymbol{L}}$, is decomposed into three components [36]:

$$\overline{\boldsymbol{L}} = \dot{\boldsymbol{F}}^p \cdot (\boldsymbol{F}^p)^{-1} = (1 - \sum_{\beta=1}^{N^{\text{tw}}} f^\beta) \sum_{\alpha=1}^{N^{\text{sl}}} \dot{\gamma}^\alpha \overline{\boldsymbol{Z}}^\alpha_{\text{sl}} + \sum_{\beta=1}^{N^{\text{tw}}} \dot{f}^\beta \gamma^\beta_{\text{tw}} \overline{\boldsymbol{Z}}^\beta_{\text{tw}} + \sum_{\beta=1}^{N^{\text{tw}}} f^\beta (\sum_{\alpha=1}^{N^{\text{sl-tw}}} \dot{\gamma}^\alpha \overline{\boldsymbol{Z}}^\alpha_{\text{sl-tw}}) \tag{12}$$

where $\dot{\gamma}^\alpha$ denotes the resolved shear strain rate on a slip system α, f^β the volume fraction of the twinned region on the twinning system β, γ^β_{tw} the (constant) twinning shear strain, and $\overline{\boldsymbol{Z}}^\beta$ is the corresponding Schmid tensor that project the strain rate contribution from the corresponding slip or twin system. The first term is the contributions of dislocation slip along N^{sl} slip systems in the untwinned region. The second term models the contribution of twinning on N^{tw} twin systems. The last term reflects the contribution from slip in the twinned regions, and $\overline{\boldsymbol{Z}}^\alpha_{\text{sl-tw}}$ is obtained through rotation of the corresponding slip system:

$$\overline{\boldsymbol{Z}}^\alpha_{\text{sl-tw}} = Q^\beta \overline{\boldsymbol{Z}}^\alpha_{\text{sl}} Q^{\beta T} \tag{13}$$

where Q^β is the rotation matrix between twinned and non-twinned lattices. Considering the fact that the deformation twins are thin structures, slip in the twinned regions are expected to be restricted to the co-planar slip systems with respect to the twin plane ($N_{\text{tw}} < N_{\text{sl-tw}}$).

Various models have been developed to describe twinning in crystals [64]. Kalidindi [36] implemented a CPFE framework, where the crystal orientation in a relaxed configuration for both the twinned and untwinned regions are pre-defined based on the initial lattice orientation. Wang et al. [74] proposed a physics-based crystal plasticity model to deal with both twinning and de-twinning mechanisms by incorporating twin nucleation, growth, shrinkage and re-twinning during the deformation process. However, many of the governing physical mechanisms for strain-induced twinning still remain unresolved [64]. Information on the evolution of the twinned volume fraction in β-HMX, especially under high rate loading is scarce. Hence, a phenomenological approach is employed in this study to describe the evolution of twin volume fraction in β-HMX [37, 74].

The evolution of twin volume fraction is taken to be affected by the resolved shear stress on the twinning systems, and the twinning resistance idealizes the resistance from neighbor molecules as well as the potential interaction between twinning and dislocation slip. Mechan-

ical twinning is taken to occur only in the positive twinning direction and no recovery of twinning (i.e., detwinning [61]) is considered. Hence, the evolution of the volume fraction of twinning depends only on the resolved shear stress and twinning resistance through a power law function [37, 74]:

$$\dot{f}^{\beta} = \frac{\dot{\gamma}^{\text{ref}}_{\text{tw}}}{\gamma^{\beta}_{\text{tw}}} \Big(\frac{\tau^{\beta}}{g^{\beta}_{\text{tw}}} \Big)^{1/m^{\beta}_{\text{tw}}} \quad \text{for} \quad \tau^{\beta} > 0 \tag{14}$$

where $\dot{\gamma}^{\text{ref}}_{\text{tw}}$ is the reference twin rate, $\gamma^{\beta}_{\text{tw}}$ is the (constant) twinning shear strain, g^{β}_{tw} is the twin resistance and m^{β}_{tw} is a rate-sensitivity parameter. The twin volume fraction induced by the permanent twin cannot be negative, and the twinned regions are not allowed to detwin, i.e., $\dot{f}^{\beta} = 0$ for $\tau^{\beta} \leq 0$. Naturally, f^{β} is always non-negative, and an upper bound in the crystals exist: $f^{\beta} \geq 0$ and $\sum_{\beta}^{N^{\text{tw}}} f^{\beta} \leq 1.0$. This phenomenological evolution law does not separate nucleation and growth of twinning, but rather tracks the volume fraction change of twinning in an average sense. The power-law parameter m^{β}_{tw} represents the strain rate sensitivity of twin growth.

2.4 Dislocation slip evolution

The first and third terms in Eq. 12 respectively define the contributions of the active slip systems and slip systems in the twinned region on the shear deformation in the crystal. A number of slip evolution models have been previously proposed for HMX [5, 7, 25, 28, 75]. At low shear stress magnitudes, the driving force on the dislocation is low and the dislocations move in a thermally activated manner. At high shear stress magnitudes, the movement of dislocations are limited by phonon drag.

In the current manuscript, slip evolution laws proposed by [7] is employed accounting for dislocation slip at slow (1e-6 m/s - 1 m/s) and faster speeds ($>$ 1 m/s) which are modeled with both thermal activation and phonon drag mechanisms. Hence, the slip rate in slip system α is expressed as:

$$\dot{\gamma}^{\alpha} = \Big(\frac{1}{\dot{\gamma}^{\alpha}_{w}} + \frac{1}{\dot{\gamma}^{\alpha}_{r}} \Big)^{-1} \tag{15}$$

where $\dot{\gamma}^{\alpha}_{w}$ and $\dot{\gamma}^{\alpha}_{r}$ respectively represent the contributions from thermal activation and phonon drag. A plot of shear stress against slip rate for each of the component relations as well as the combined behavior, and using the fit parameters, is given in our previous work [85]. The thermally activated slip is expressed as:

$$\dot{\gamma}^{\alpha}_{w} = \begin{cases} \dfrac{\dot{\gamma}^{\alpha}_{wo}}{\sqrt{\rho_{\text{norm}}}} \Big[\exp\big(-\dfrac{\Delta G^{\alpha}(\tau^{\alpha})}{\kappa\theta} \big) - \exp\big(-\dfrac{\Delta G^{\alpha}(-\tau^{\alpha})}{\kappa\theta} \big) \Big] + h(\tau^{\alpha}), & \text{if} \quad |\tau^{\alpha}| \leq g^{\alpha} \\ \dfrac{\dot{\gamma}^{\alpha}_{wo}}{\sqrt{\rho_{\text{norm}}}} \text{sign}(\tau^{\alpha}) \Big[1 - \exp\big(-\dfrac{2c_G \mu^{\alpha}}{\kappa\theta} \big) \Big] + h(\tau^{\alpha}), & \text{if} \quad |\tau^{\alpha}| > g^{\alpha} \end{cases} \tag{16}$$

where $\dot{\gamma}^{\alpha}_{wo}$ is the reference shear strain rate, κ is the Boltzmann constant and θ the temperature. The transition from thermal activation to phonon drag is controlled by the penalty function: $h(\tau^{\alpha}) = \text{sign}(\tau^{\alpha})(\frac{\tau^{\alpha}}{g^{\alpha}})^{\zeta}$ where ζ is a parameter. When $\tau^{\alpha} > g^{\alpha}$, the penalty func-

tion significantly increase the resolved shear strain rate of thermal activation, and reduces the relative contribution of thermal activation in the overall resolved shear strain rate. ρ_{norm} is a dimensionless dislocation density measure normalized by the reference dislocation density ρ_{ref} ($\rho_{\text{norm}} = \rho/\rho_{\text{ref}}$). $\Delta G^{\alpha}(\tau^{\alpha})$ is given by:

$$\Delta G^{\alpha}(\tau^{\alpha}) = c_G \mu^{\alpha} \Big[1 - \Big(\frac{\tau^{\alpha}}{g^{\alpha}}\Big)\Big]^{q} \tag{17}$$

where c_G, q are constants, and μ^{α} is the shear modulus resolved in the α^{th} slip system [24]. g^{α} is the slip strength of the slip system α, and takes the form:

$$g^{\alpha} = r^{\alpha}(g_o + s\sqrt{\rho}) \tag{18}$$

where, s and g_o are model parameters, and r^{α} is the ratio of the slip system strength g^{α} and the reference slip system strength, $g^{(010)[100]}$ ($r^{(010)[100]} = 1$).

For the glide of dislocations between sets of obstacles, the slip rate is governed by the drag term [4]:

$$\dot{\gamma}_r^{\alpha} = \text{sign}(\tau^{\alpha}) \dot{\gamma}_{ro} \rho_{\text{norm}} \Big[1 - \exp(-\frac{|\tau^{\alpha}|}{D_r})\Big]; \quad D_r = D_{ro}\frac{\theta}{\theta_0} \tag{19}$$

where $\dot{\gamma}_{ro}$ is the reference shear strain rate, D_{ro} is the reference drag stress, and θ_0 is the reference temperature. The evolution of slip strength is controlled by the dislocation density which, under dynamic loading, evolves through generation and annihilation mechanisms:

$$\frac{d\rho}{d\gamma} = n_1\sqrt{\rho} - n_2 \dot{\gamma}^{-\frac{1}{n_3}} \rho \tag{20}$$

n_1, n_2 and n_3 are constants. The initial dislocation density is taken from [7] and consistent with experiments discussed in Ref. [67].

Molecular packing of β-HMX [54] induces slip asymmetries in all slip planes. The slip asymmetry was also observed in other energetic molecular crystals, such as RDX [48]. While modeling of asymmetry is straightforward from the implementation viewpoint, values for asymmetric critical resolved shear stress (CRSS) and mobility are not currently available. Slip asymmetry effects are therefore not included in the present model.

ABAQUS has been employed in this study as the finite element solver, and the above constitutive model is implemented using the user supplied subroutine VUMAT. The overview of the stress update implementation is as follows: the velocity gradient $\boldsymbol{L}$ at t_{n+1} is given, and it is used in Eq. 5a and Eq. 5b to update $\overline{V}'_{n+1}$ and J_{n+1}. The deviatoric strain ($\overline{E}'_{n+1}$) and volumetric strain ($\overline{E}_{V,n+1}$) are then updated using Eq. 4. The plastic velocity gradient is obtained through Eq. 12, Eq. 14 and Eq. 15. Equation 6 is employed to compute W^R which is used to compute $\boldsymbol{R}_{n+1}$ through exponential map. With the updated strains and elasticity model in Section 2.2, stress is updated at t_{n+1} as well (Eq. 7 and Eq. 8). Under the loading rates considered in this manuscript, the adiabatic assumption is employed for temperature

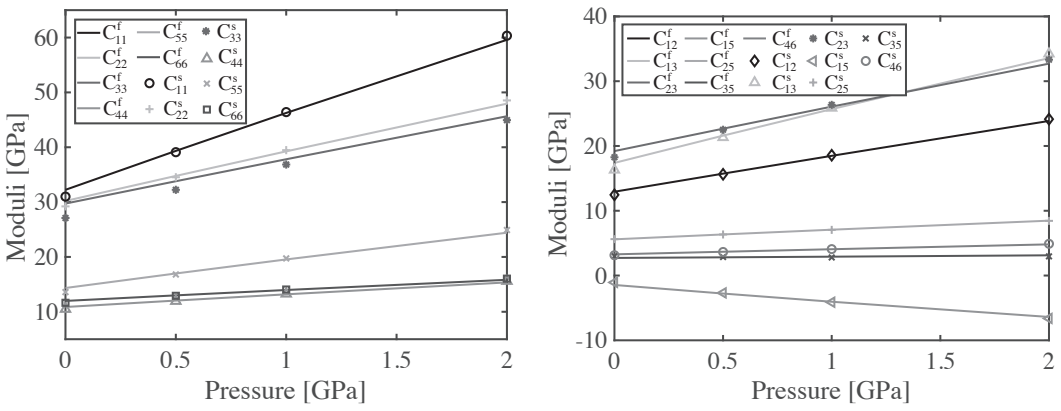

(a) (b)

Figure 1: Elasticity coefficients with pressure dependency for (a) the diagonal terms; and (b) the off-diagonal terms.

rise. The updated dissipation induced by the viscoplastic slip, twinning and pressure-volume work at t_{n+1} are used to update temperature.

3 Parameter Calibration

In this section, data from previous experimental studies, molecular dynamics (MD) and CPFE simulations are employed to calibrate the parameters of the proposed model for β-HMX. Calibration of the parameters for the anisotropic elasticity model and EOS, dislocation slip evolution, and twinning evolution are discussed separately.

3.1 Elasticity

The elastic model is fully described by the elasticity coefficients, mass density, specific heat, EOS parameters and the Gruneisen tensor. Thirteen coefficients of the anisotropic tensor of the monoclinic lattice are pressure dependent. Mathew and Sewell [49] computed the elasticity tensor components using MD simulations for pressures up to 2 GPa, as shown in Fig. 1. These values are used in the model calibration.

The EOS and the Gruneisen tensor account for the large volumetric deformation and potential distortion induced by thermal expansion. Bulk modulus, B_0, and the derivative of the bulk modulus with respect to pressure, B_0', are taken to be 16.71 GPa and 7.79 following [43]. The Gruneisen tensor for the anisotropic material is expressed as a function of mass density, specific heat and thermal expansion coefficients. Initial mass density of β-HMX, ρ_0^{mass}, is 1.9 g/cm^3, and the specific heat c_V is set to 1 kJ/(kg·K). Thermal expansion coefficients are obtained from the measurements of Ref. [29] and summarized in Table 1.

Table 1: Parameters of the elasticity model.

Parameter	B_0	B_0'	c_V	ρ_0^{mass}	α_{11}
Unit	GPa		kJ/(kg · K)	g/cm^3	10^{-6}/K
Value	16.71	7.79	1	1.9	-2.9
Parameter	α_{22}	α_{33}	α_{23}	α_{13}	α_{12}
Unit	10^{-6}/K	10^{-6}/K	10^{-6}/K	10^{-6}/K	10^{-6}/K
Value	116	17.9	0	-12.6	0

Table 2: Slip strength ratios.

Slip system	(010)[100]	(011)[100]	$(01\bar{1})[\bar{1}00]$	$(101)[0\bar{1}0]$	(001)[100]
Ratio r^α	1	0.963	0.963	0.933	1.68
Slip system	$(101)[10\bar{1}]$	$(011)[\bar{1}1\bar{1}]$	$(0\bar{1}1)[111]$	$(1\bar{1}0)[001]$	$(\bar{1}\bar{1}0)[00\bar{1}]$
Ratio r^α	0.376	0.931	0.931	0.701	0.701

3.2 Dislocation slip parameters

Previous experiments and first principles calculations suggest that slip in HMX molecular crystal can occur along a large number of slip systems induced by the irregular molecular shape. Potential slip systems in β-HMX have been identified by Gallagher et al. [23] as (001)[100], $(101)[10\bar{1}]$ and (101)[010]. Barton et al. [7] employed ten slip systems determined based on MD simulations. In that work, the corresponding slip strengths were selected according to an optimization algorithm to minimize the difference between simulation predictions and experimental observations. Recently, Pal and Picu [54] used MD simulations to identify slip systems which are potentially active in β-HMX, and ranked them in terms of their propensity for slip. Khan et al. [39] extended their study to finite temperatures, and evaluated critical thresholds for activating steady-state dislocation motion in the two most probable slip planes, (101) and (011). Zhou et al. [86] identified eight potential slip systems from ReaxFF-lg reaction dynamic simulations subjected to shock loadings normal to (110), (011), and (010) planes. To model the nature of plasticity in HMX, full list of active slip systems and accurate description of slip behaviors within each slip system are needed from either smaller scale information or through parameter calibration at the continuum scale.

We initially attempted to calibrate parameters for all potential slip systems (27 systems) proposed in the literature [7, 39, 48, 54, 55, 86]. However, incorporating more slip systems than those used in Barton's model complicates the calibration procedure, and no substantial improvement in matching particle velocity profiles is observed. Therefore, instead of modeling full list of potential slip systems, ten slip systems proposed by Barton et al. [7] are employed in the current manuscript and summarized in Table 2 with calibrated parameters through particle velocity profiles. All slip systems are given in $P2_1/n$ notation. The lattice structure of β-HMX is described by four cell parameters: a, b, c and β (a=6.5374 Å, b=11.0296 Å, c=7.3549 Å, and β=102.69° [13]). Slip system strength ratios r^α and phonon drag parameter D_{ro} as well as the thermal activation and dislocation density evolution parameters are set to those provided in

Table 3: Flow rule and hardening rule parameters.

Parameter	$\dot{\gamma}_{wo}$	c_G	g_0	s	q	$\dot{\gamma}_{ro}$	D_{ro}	ζ
Value	1	11.47	103	0.1666	1	2.5	1160	150
Unit	μs^{-1}	K/MPa	MPa	MPa· mm		μs^{-1}	MPa	
Parameter	n_1	n_2	n_3	η	θ_0	ρ_0	ρ_{ref}	
Value	37.99	62	4.98	0.9	293	0.0307	0.452	
Unit	mm^{-1}				K	μm^{-2}	μm^{-2}	

Ref. [85].

3.3 Twinning parameters

The primary twinning system in HMX crystal has been identified as $(101)[10\bar{1}]$ in $P2_1/n$ space group [2, 12, 23, 56] ($N^{\text{tw}} = 1$). Within the twinning system $(101)[10\bar{1}]$, characteristic twinning shear strain γ_{tw}, reference twin rate $\dot{\gamma}_{\text{tw}}^{\text{ref}}$, twinning resistance g_{tw} and the power-law parameter m_{tw} fully define the twinning evolution law. The fact that deformation twins are thin structures constrains further slip and twinning in the twinned region. The contribution of twinning at high strain rate regime has not been experimentally investigated for HMX in a quantitative fashion that allows full calibration of all associated material parameters. The issue is exacerbated by a lack of signature features in the high rate response of the specimens that are directly attributed to twinning. The calibration of the twin related parameters therefore contains a degree of uncertainty.

$\gamma_{\text{tw}} = 0.242$ is calculated with the lattice parameters and twinning system stated above using the procedure provided in [42]. While research has been done to quantify twinning resistance, g_{tw}, for other materials [52], there is no experimental measurement of this parameter for HMX. Zamiri and De [80] employed a slip-like twinning model with the initial value of twinning resistance 2.5 MPa at 24 °C and 2.2 MPa at 55 °C. and the saturation values of twin resistance are also reported as 2.55 MPa at 24 °C (297 K) and 3.1 MPa at 55 °C (328 K). The study by Zamiri and De [80] used identical values for twinning and slip resistance. A commonly used method to calibrate the critical stress is through fitting the macroscopic stress-strain curve [33, 34, 46, 52, 60, 71]. However, this approach is not applicable for β-HMX due to the lack of experimental stress-strain curve at the relevant strain rates. The rate-sensitivity parameter m_{tw} is set to a small number (0.05) to approach the rate-insensitivity for twinning [33, 36, 60].

Two of the twinning parameters (reference twin rate $\dot{\gamma}_{\text{tw}}^{\text{ref}}$ and twinning resistance g_{tw}) are calibrated using the plane shock experiments by Dick et al. [20]. In these experiments, an initial velocity is applied to an impactor. The shock wave generated by the impactor is transmitted through the specimen, which is a single HMX crystal. The calibration is performed by minimizing the discrepancy between experimentally observed and numerically simulated particle velocity profiles at the interface between the specimen and the PMMA window behind the specimen.

Table 4: Loading data.

Shot no.	Sample type	Thickness (mm)	Impactor Velocity (km/s)
1180	110	1.23	0.3185
1166	110	3.18	0.3068
1182	110	3.57	0.5209
1181	011	1.39	0.3160
1068	011	3.00	0.3140
1168	011	4.66	0.3132

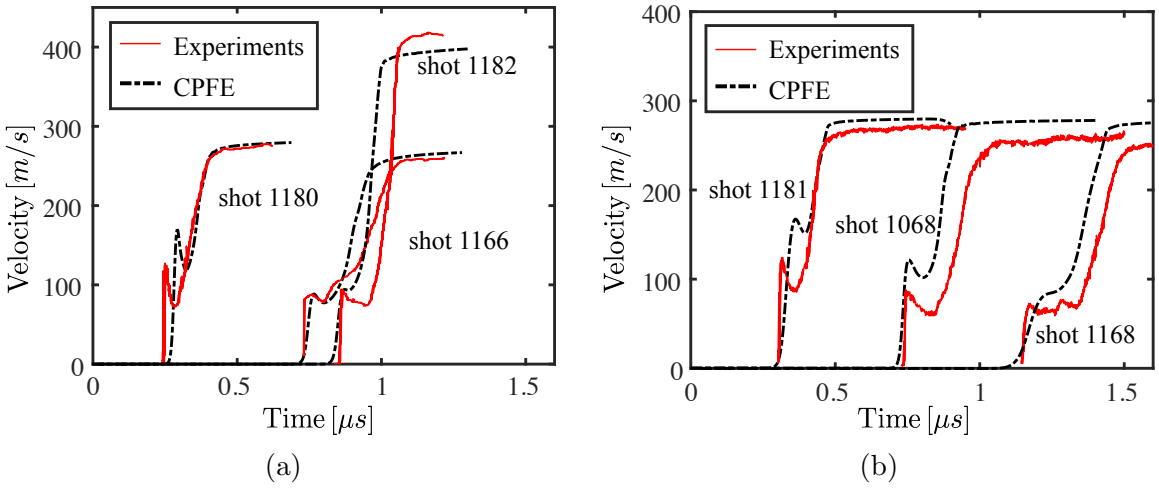

Figure 2: Model verification with respect to loading in (a) the $(110)_{P2_1/n}$ direction; and (b) the $(011)_{P2_1/n}$ direction.

In the numerical simulations, the specimen is discretized using a quasi-one-dimensional mesh (element size 0.01 mm), and the loading is applied as prescribed constant velocity. The amplitude of the applied velocity on the HMX specimen is determined using the measured impactor velocity through the impedance matching technique, in which linear Hugoniot relationships are employed for the impactor, anvils and HMX [9, 51]. The PMMA window is bonded to the HMX specimen, and modeled using the nonlinear viscoelastic constitutive law developed by Schuler and Nunziato [65]. Periodic boundary conditions are applied at the top/bottom and front/back boundaries. Dislocation density field is taken to be uniform prior to the onset of the dynamic load. The particle velocity at HMX/PMMA interface is extracted for parameter calibration. In a similar study, Barton et al. [7] observed a discrepancy between the times of arrival in the predictions and experiments due to the dependence of elastic parameters to pressure and temperature and reported the prediction results with a time shift. Time shift is not used. In the current study, the elastic moduli of the crystal are taken to be pressure dependent based on the data shown in Fig. 1. Time shift idea has not been used and pressure dependent moduli provides sufficiently accurate time of arrival as shown in Fig. 2. It is also noteworthy that Fig. 1 indicates a slight pressure dependency of the shear moduli. The

slight pressure dependency has only a minor influence on the speed of the plastic wave.

Calibration data are collected from three shots along $(110)_{P2_1/n}$ direction and three shots with single crystals along $(011)_{P2_1/n}$ direction as shown in Table 4. Experiments along $(010)_{P2_1/n}$ direction are not used for calibration due to the fact that the plane and direction of twinning are perpendicular to the impact plane therefore no twinning deformation is expected. In the calibration process, strong crystal orientation dependency of the twin model is observed. Prevalent twin accumulation occurs at shots under loading in (011) direction, while only a small amount of twin is observed in (110) direction. The predictions of the calibrated model and experimental measurements are compared in Fig. 2. Overall, a reasonable agreement between the predictions and experimental data is observed. Elastic precursor decay is observed in both loading directions. For instance, in (011) direction, the amplitude of the elastic wave reduces from 160 m/s to 70 m/s when the wave travels from 1.39 mm to 4.66 mm. Although these curves are obtained from different impact experiments, the amplitudes can be used to analyze the reduction of elastic precursor considering the minor difference between impactor velocities (less than 1%). Elastic precursor decay is due to the plastic dissipation when the material is being compressed [3, 15, 17, 57, 70], and the dissipation has been correlated with dislocation density and dislocation velocity in Orowan's equation. In the current model, the dissipation is controlled by the resolved shear strain rate in slip systems and twin volume fraction in the twin system. The predicted peak steady particle velocities exhibit moderate discrepancy in shots 1182, 1068 and 1168. This is attributed to shortcomings of the PMMA constitutive model [65] in capturing large volumetric deformation in shock condition. The finite width of the elastic wave observed in Fig. 2 is due to the artificial viscosity employed in FEA solver [35, 72]. The aforementioned experimental study also included data on (010) specimens. Since twinning is not activated on (010) specimens, the predictions with or without the twinning model are identical. These results are not included in this manuscript. Furthermore, we observe slightly larger deviation in prediction of time of arrivals in the (010) direction compared to the experimental observations, indicating some uncertainty in the elastic constants and the EOS.

Calibrated twinning parameters are summarized in Table 5. Although the prediction of overall wave propagation is qualitatively similar to the prediction with a previous model that considered only slip evolution on the twin plane [85], the presence of twins does contribute to the plastic response, which is explained in Fig. 3. The particle velocity profile of shot 1168 is simulated with two models, and the fittings are shown in Fig. 3a. In the first model, only dislocation slip is incorporated in the current large deformation CPFE model, while in the second model, both dislocation slip and twins are considered. All slip parameters are identical in the two models. The presence of twins reduces the elastic peak at t=0.15 μs, and increases the following stress decay. The plastic peaks in both models are the same, while velocity of the plastic wave is observed to be slower in the model with twinning than the prediction without twins for shots in (011) direction. Figure 3b shows the comparison for shot 1181, where the sample is shorter than that for shot 1168 but with identical orientation and similar impact

Table 5: Twinning parameters.

Variable	$\dot{\gamma}_{\text{tw}}^{\text{ref}}$	γ_{tw}	m_{tw}	g_{tw}
Unit	μs^{-1}			MPa
Number	1	0.242	0.05	120

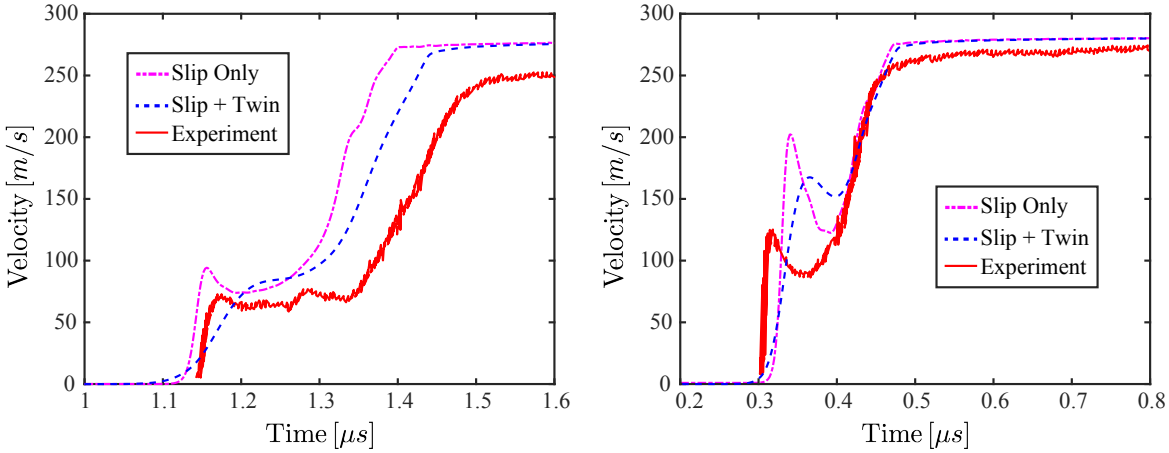

Figure 3: Effect of twinning on model prediction. Particle velocity of (a) shot 1168 and (b) shot 1181 are predicted using current model with twinning (dislocation slip and twin) and without twinning behavior (dislocation slip only).

velocity. In this case, the presence of twins appears to have relatively small effect on the velocity profile. Although the reduction of the plastic wave velocity induced by twinning is larger at the beginning of wave propagation, the resulting plastic wave arrival time becomes more obvious as the wave propagated deeper into the material due to the accumulative effect of the plastic behavior. The elastic peak and plastic wave propagation is better captured, while the predictions of initial slope and the shape of the elastic precursor are not improved when twinning is activated.

4 Analysis of twin evolution

4.1 Single crystal configuration

In what follows a deeper investigation on the evolution of twinning in single crystal configuration is performed. The numerical investigation uses the setup employed in model calibration described above.

4.1.1 Effect of crystal orientation

Mechanical twinning is prevalent when the resolved shear stress (RSS) in $(101)[10\bar{1}]$ direction exceeds the twinning resistance. This implies that twinning is not sensitive to deformation in certain directions (where RSS is low or negative) and sensitive to deformation in others (where

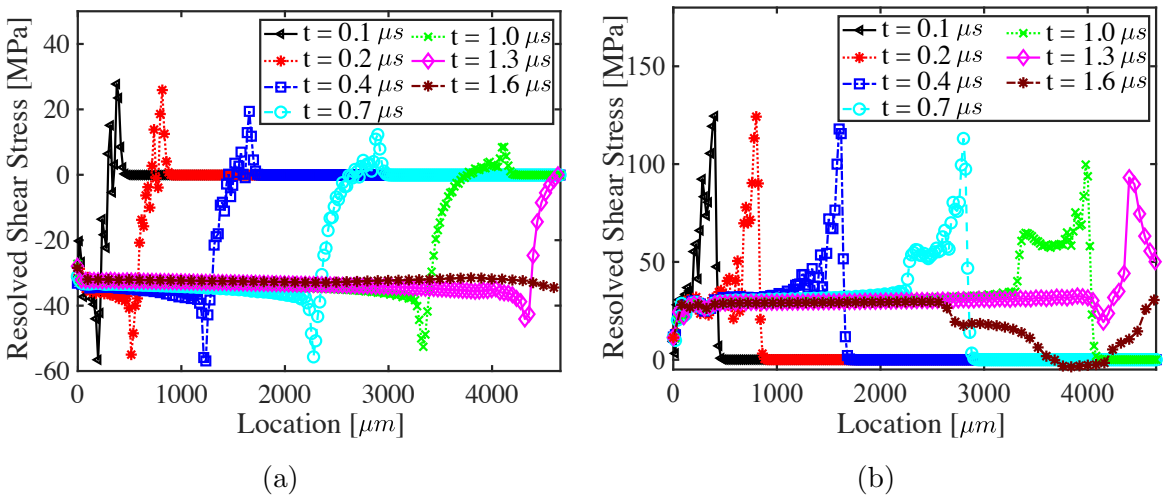

Figure 4: Orientation dependency of resolved shear stress in (a) the $(110)_{P2_1/n}$ direction; and (b) the $(011)_{P2_1/n}$ direction. Temporal evolution of RSS is plotted at t=0.1 μs, 0.2 μs, 0.4 μs, 0.7 μs, 1.0 μs, 1.3 μs and 1.6 μs. Location x=0 mm represents the left hand side of the specimen, and x=4.66 mm represents the HMX/PMMA interface.

RSS is positive and high). In the current study, the mechanical twinning is investigated when the compression wave aligns with two crystal orientations: (110) and (011), one of which promotes higher level of twinning.

Employing the setup of the calibration experiments, a 4.66 mm long single crystal HMX specimen is subjected to prescribed boundary velocity of 200 m/s. The spatial distributions of the resolved shear stress and twin volume fraction on twin system are recorded at seven time instances (i.e., t=0.1 μs, 0.2 μs, 0.4 μs, 0.7 μs, 1.0 μs, 1.3 μs and 1.6 μs) and plotted in Figs. 4 and 5. The effect of loading orientation on the stress evolution on the twin system is evident from the differences in the (011) direction (Fig. 4b) and the (110) direction (Fig. 4a). In Fig. 4a, specimen deformation in $(101)[10\bar{1}]$ follows the stress wave which passes through the specimen without significantly changing shape, and reaching a stable state (RSS $\approx$ -33 MPa) on the wake of the wave. In contrast, a more complex stress evolution is observed in Fig. 4b. Between 0 μm and 1000 μm, RSS exhibits a double peak structure once the dynamic wave has already passed. Similar structure is also observed in the particle velocity profiles, and represents the separation of elastic and plastic waves. Constant stress state is reached between $\sim$500 μm and the wave front. Resolved shear stress in (110) case does not exceed 120 MPa during the entire dynamic deformation process, which leads to no twin formation. However, RSS in (011) exhibits a large peak ($>$ 120 MPa) which directly induce twin accumulation until the RSS drops below the twinning resistance (120 MPa). RSS behind the shock front is positive but lower than the resistance. At t=1.3 μs, the wave has already reflected at the HMX/PMMA interface thus the double peak structure disappears.

Figure 5 shows the twin volume fraction profile at a number of time instances for the (011) specimen loaded at 200 m/s velocity (Fig. 5a) and 500 m/s velocity (Fig 5b). The shock front

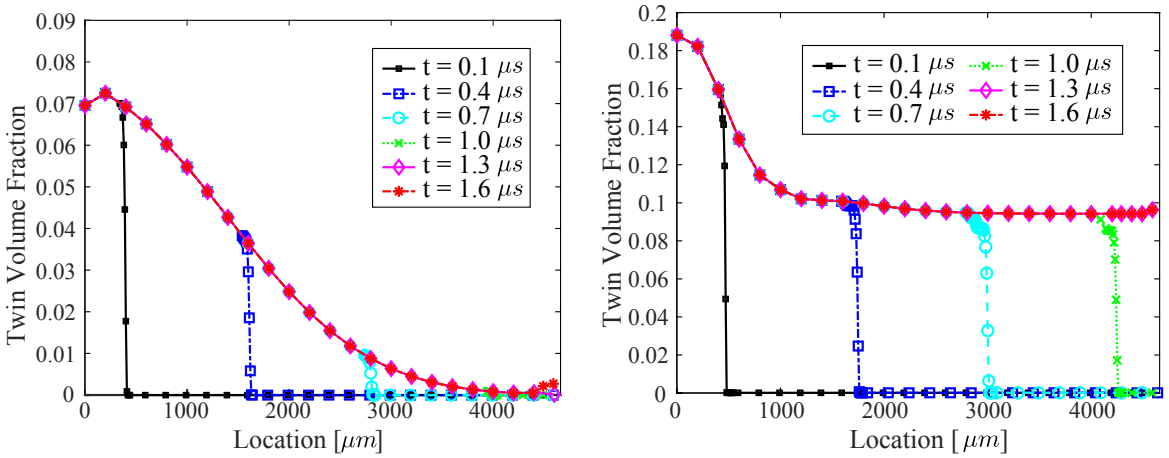

Figure 5: Temporal evolution of twin volume fraction at loading (1) 200 m/s, and (2) 500 m/s. Loading is along (011) direction.

is marked by the sudden increase in twinning activated by the high RSS observed at the shock front. Twinning rapidly accumulates when the resolved shear stress approaches or exceeds twinning resistance. The twin volume fraction increases from zero to a decreasing peak as the shock front propagates through the specimen. As shown in Fig. 5a, at t=0.1 μs, the wave arrives at approximately 400 μm (Fig. 5a) and the induced twin volume fraction is approximately 7.25%. At 0.4 μs, 0.7 μs and 1 μs, the induced twin volume fraction reduces to 3.5%, 0.78% and 0.08%, respectively. After the shock is reflected back at the HMX/PMMA interface, due to the relatively small impedance contrast, a slight increase in the twin concentration is observed. A similar phenomenon is observed in Fig. 5b.

We also observe the propagation of transition region after shock front. The twinning transition region is defined as the distance it takes for the twin to fully form at the shock front. Under 200 m/s loading at t=0.1 μs, the twinning transition region starts at x=350 μm and ends at x=411 μm. At t=0.4 μs and t=0.7 μs, the transition region remains as 60 μm. The propagation of the transition region without significant size change indicates stable energy dissipation process at the wave front.

4.1.2 Effect of impact velocity

The same specimen configuration (shot 1168) and boundary conditions as above are employed to study the response when subjected to different loading velocities in the (110) direction. At high impact velocity (500 m/s), compared with twinning at lower loading velocity (200 m/s, as shown in Fig. 5a), more twins are observed, and twinning accumulation reaches a steady state. The twinning transition regions at t=0.1 μs, t=0.4 μs, t=0.7 μs and t=1.0 μs increase to 60 μm, 160 μm, 220 μm and 260 μm at 500 m/s load velocity. The expansion of transition region at the higher impact velocity and more accumulated twins clearly indicate increased energy dissipation at the wave front and more plastic deformation when the impact velocity

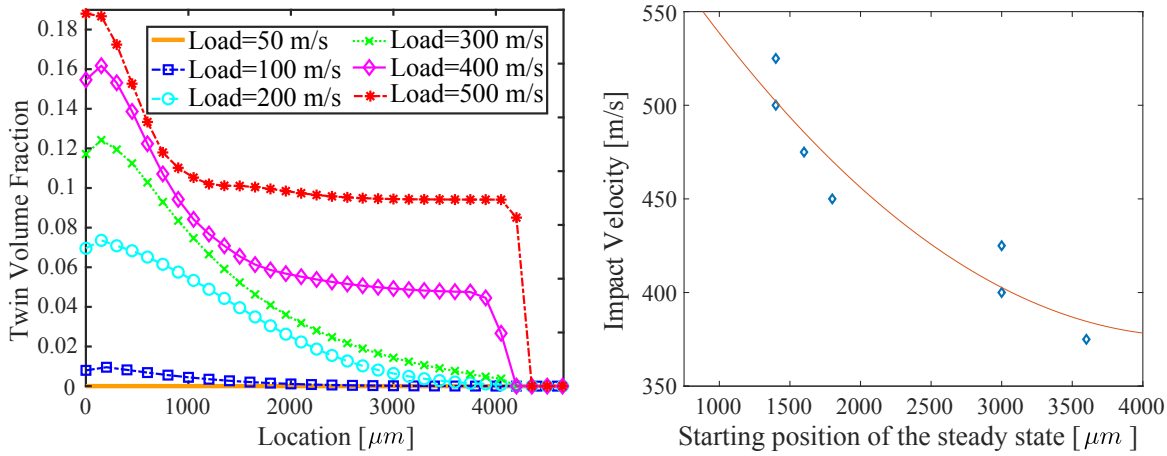

(a) (b)

Figure 6: (a) Twin volume fraction in single crystal when the wave arrives at the HMX/PMMA interface for loading velocities of 50 m/s, 100 m/s, 200 m/s, 300 m/s, 400 m/s and 500 m/s. (b) Starting locations of the steady state for impact velocities of 375 m/s, 400 m/s, 425 m/s, 450 m/s, 475 m/s, 500 m/s and 525 m/s when the change of twin volume fraction is constant (5e-6/μm).

increases.

Figure 6a shows the spatial distribution of twin volume fraction when the dynamic wave arrives at the HMX/PMMA interface (1.050 μs, 1.042 μs, 1.032 μs, 1.020 μs, 1.010 μs and 1.000 μs under impact velocities of 50 m/s, 100 m/s, 200 m/s, 300 m/s, 400 m/s and 500 m/s). It is clear that twin volume fraction increases with the loading rate, and the maximum amount of twinning occurs near the loading boundary (x≈0 μm). Maximum twin volume fraction $f_{\max}$ in 50 m/s case is less than 0.01%, while $f_{\max}$ in 500 m/s case reaches 18.8%. Other cases (400 m/s, 300 m/s, 200 m/s and 100 m/s) have maximum twin fractions 16.17%, 12.42%, 7.36% and 0.95%, respectively. Especially at higher impact velocities, a boundary region develops with high twin fraction that attenuates to a steady value in the sample interior. The attenuation is slower at lower load rates. The iso-line plotted in Fig. 6a demonstrates the nonlinear relationship between the "run-to-steady-state" and the load rate. Points on the iso-line indicate the location (x-axis in Fig. 6a) beyond which no substantial change (quantified by threshold of 5e-6/μm) in the twin volume fraction is observed. The steady state for 500 m/s case starts at approximately x=1 mm with $f \approx 10\%$, while in 400 m/s case, the steady region ($f \approx 5.5\%$) starts at 2 mm. Steady state region is not observed in the cases with lower applied velocities. To further depict the evolution of the steady state starting position as a function of impact velocity, the iso-line is also plotted in Fig. 6b with additional impact velocities of 375 m/s, 425 m/s, 450 m/s, 475 m/s, and 525 m/s.

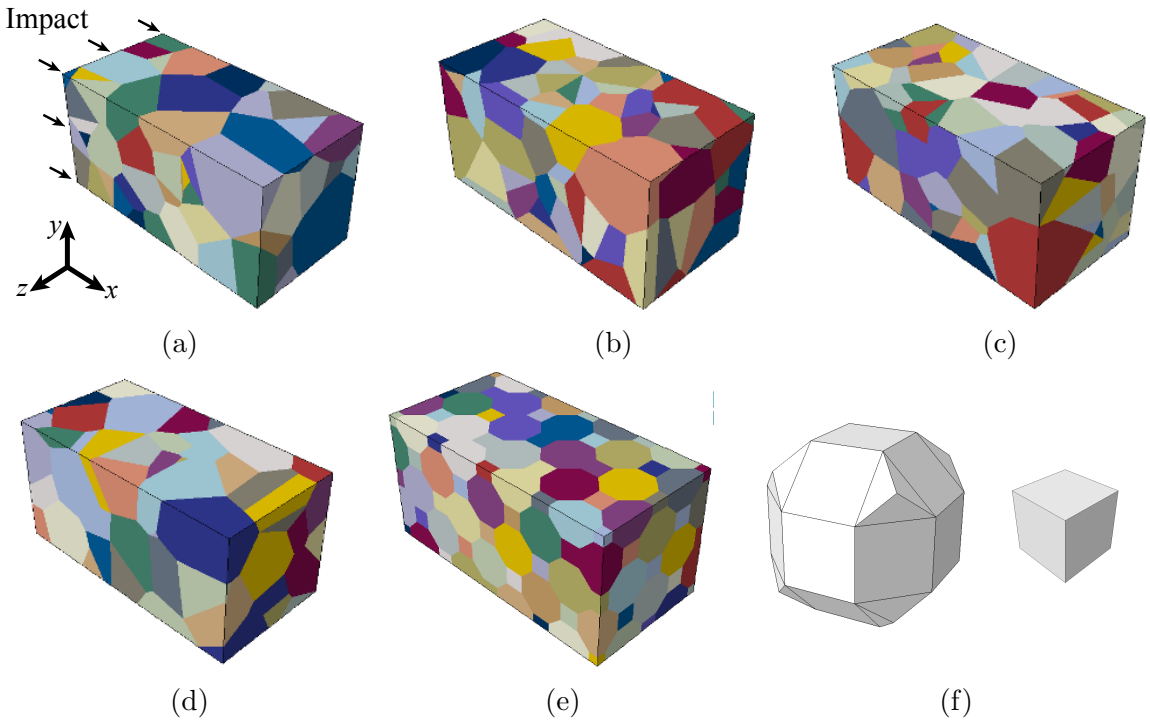

Figure 7: Microstructures of polycrystal configuration. Each colored region represents a single crystal particle. Impact velocity is applied on the left hand side, and the movements of top, bottom, front and back faces are constraint in their normal directions.

4.2 Polycrystal configurations

Particle-particle interactions could lead to stress and strain concentrations in an energetic material mesostructure, and have potential links to hot-spot formation [21]. In this section, we investigate twinning in polycrystalline HMX configurations under impact loading. Polycrystalline HMX is typically synthesized to a compressed granular form or bound by a polymeric binder with small binder concentration. In the former, the mesostructure includes interparticle voids, whereas in the latter, the void spaces are completely or partially filled with the binder. The current study does not include the presence of voids or binder, and focuses on the twin formation in idealized mesostructures with particles fully bonded with each other. Similar assumptions have been previously employed to investigate polycrystalline energetic particles, see e.g. [28].

4.2.1 Mesoscale structures

The mesoscale morphologies, the boundary and loading conditions considered in the mesoscale simulations are shown in Fig. 7. Five mesoscale specimens subjected to high rate compression loading are investigated in this study. Each particle that comprise the mesoscale morphologies is idealized as a single crystal. The size of the numerical specimens is 400 μm $\times$ 400 μm $\times$ 800 μm. The orientation of each particle is sampled from a uniform random distribution.

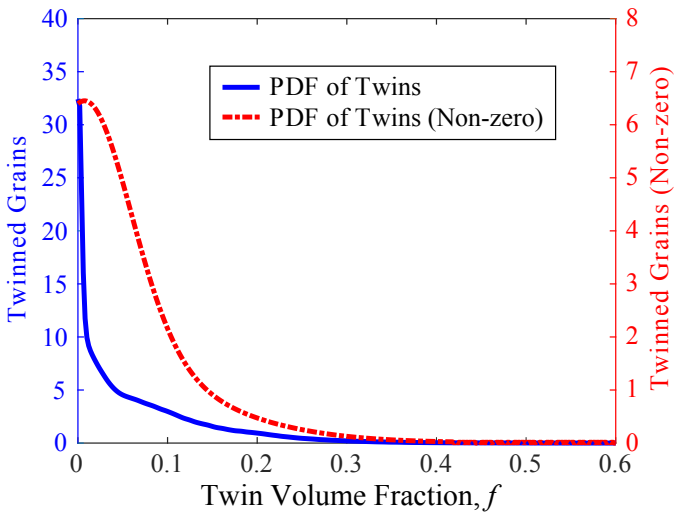

Figure 8: Probabilistic distribution of maximum twin volume fraction in each grain (solid curve) and maximum twin volume fraction in each grain excluding grains where twinning is not observed (dash curve).

The three Euler angles (Kocks convention) defining the orientation of a crystal is assumed to be independent of each other, and sampled from the range of $0 < \Phi_1 < 2\pi$, $0 < \phi < \pi$ and $0 < \Phi_2 < 2\pi$. The loading is imparted on the specimens as prescribed velocity as shown in Fig. 7a. The displacements on the front/back/top/bottom faces are constrained in the normal directions, and free in other directions.

Four of the five mesostructures (Figures 7a to 7d) include randomized polygonal particle geometries. The mesostructures are generated using the Neper software [62]. A bimodal particle size distribution (see Ref. [85]) is used to create these four mesostructures, each of which consists of 120 grains. The geometries are therefore four realizations with identical morphological statistics. Note that variation in the dynamic response is expected as the mesostructures are not large enough to be statistically representative. Alternatively, we aggregate the responses leveraging the statistical volume concept in the analyses. The fifth microstructure, shown in Fig. 7e, is constructed by tiling two polyhedral particle shapes (Fig. 7f) in a regular pattern. Similar, geometrically regularized mesostructures, have been employed in previous studies to investigate the dynamic response of energetic materials (e.g. Ref. [28]). The mesostructures are discretized with approximately 500,000 - 1 million trilinear tetrahedral elements. Simulations are conducted using dynamic explicit finite element method. Time step sizes are chosen to ensure stability (3×10^{-6} - 1×10^{-5} μs).

To understand the overall twinning evolution, the collective distributions for twin volume fractions from the first four cases (Figures 7a to 7d) are plotted in Fig. 8 under the excitation amplitude of 250 m/s. The blue solid line in Fig. 8 represents the probability distribution of the maximum twin volume fraction reached during the simulation in each grain. The large PDF value near f=0 indicates that large portion of the specimens (32.5% volume or 156 grains),

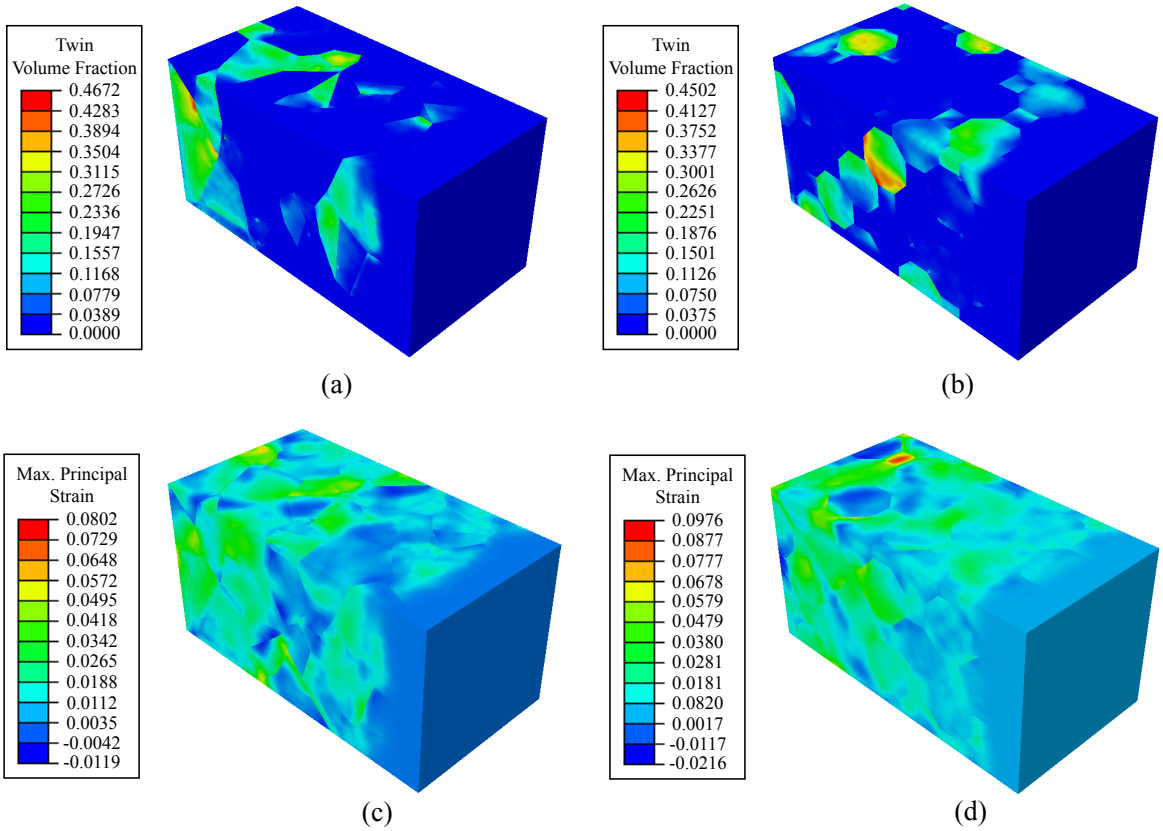

Figure 9: Twin volume fraction distribution of the mesostructures with (a) randomized polygonal particle geometries and (b) regularized particle geometries, and maximum principal strain with (c) randomized polygonal particle geometries and (d) regularized particle geometries at t=1.6 μs.

do not exhibit or exhibit a very small amount of twinning. After excluding these grains with zero maximum twin volume fraction, the PDF of maximum twin volume fraction is plotted in red dash line. The critical regions of high twin concentration only exist in a limited number of locations in the mesostructure.

Figure 9 illustrates the twin volume fraction and maximum principal strain contours as predicted using the mesostructures with random (Fig. 7b) and regular (Fig. 7e) particle geometries when the shock wave front is near the end of the specimens. In both types of mesostructures, high twin concentrations are observed at or near particle boundaries, which indicates the roles of interparticle misorientation and particle geometry on twin formation. Although the twin accumulation regions are likely to have relatively high strain concentration, a high strain region does not imply high twin volume fraction. The local regions with peak twin concentration in both mesostructures as well as the grain orientations are shown in Fig. 10. High twin concentration regions are observed both at the boundary (Fig. 10) and the interior of the mesostructures (Fig. 13a and Fig. 13d). In the mesostructure with polygonal particles, $f_{\max} = 0.4673$ occurs at a triple junction on the boundary as plotted in Fig. 10a. In the

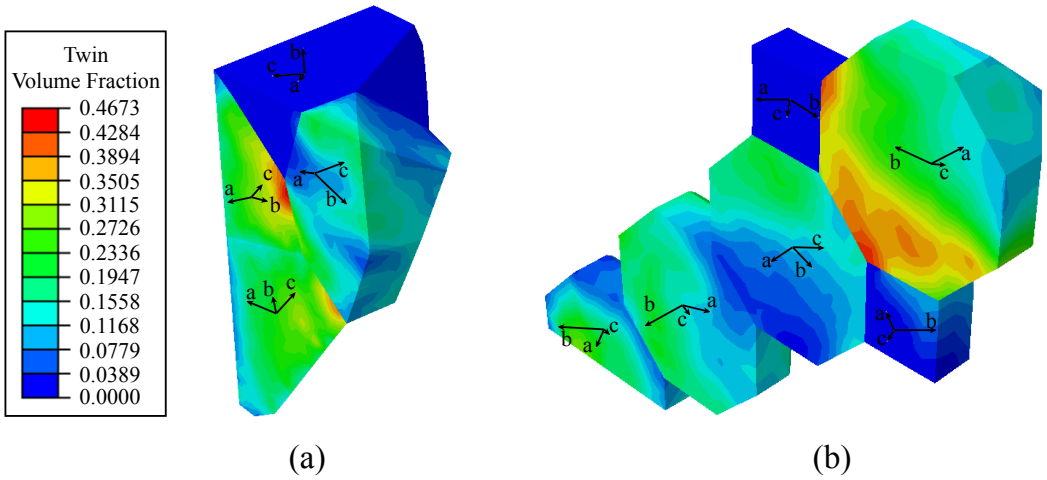

Figure 10: Local region of twin concentration for mesostructures with (1) randomized polygonal particle geometries and (2) regularized particle geometries at t=1.6 μs. Lattice axes $\boldsymbol{a}$, $\boldsymbol{b}$ and $\boldsymbol{c}$ for each grain are plotted as well. The lattice axes are not orthogonal due to the monoclinic lattice structure.

mesostructure with regularized particles, a column of particles aligning on the front face show high twin volume fraction, with $f_{\max} = 0.4502$ observed again at a triple junction (Fig. 10b).

Although grain misorientations appear to characterize the local twinning initiation and accumulation behavior, the peak twin volume fraction does not show a clear connection to the grain misorientation angles. In both Fig. 10a and Fig. 10b, the highly twinned grain is next to a grain that has only a small amount of twinning, which seems to suggest an effect of crystal misorientation and grain boundary. To investigate the possible effect of grain misorientation between neighboring particles, maximum twin volume fraction discrepancy (TVFD) between each neighbor grain pair is plotted in Fig. 11 where mean and standard deviation are computed in five intervals for mesostructures with randomized polygonal particle geometries and regularized polygonal particle geometries. The means of twin volume fraction discrepancy exhibit small values ($< 9\%$) for all grain pairs in two mesostructures, while the standard deviation are larger than the means, which indicates that misorientation is not clearly connected to twin concentration. In the both mesostructures, mean and standard deviation of the twin volume fraction discrepancy do not show a strong dependence on the misorientation angle.

4.2.2 Loading velocity

The mesostructure shown in Fig. 7b is subjected to four different impact velocities (100 m/s, 200 m/s, 300 m/s and 400 m/s) to investigate twinning evolution at different deformation rates. The simulations are performed until the shock front reaches the face of the mesostructure opposing the impacted face. Total time of the simulations are 0.5 μs, 0.25 μs, 0.17 μs and 0.15 μs for impact velocities of 100 m/s, 200 m/s. 300 m/s and 400 m/s, respectively. The corresponding time step size are 2.5e-5 μs, 1.25e-5 μs, 5e-6 μs and 1e-6 μs.

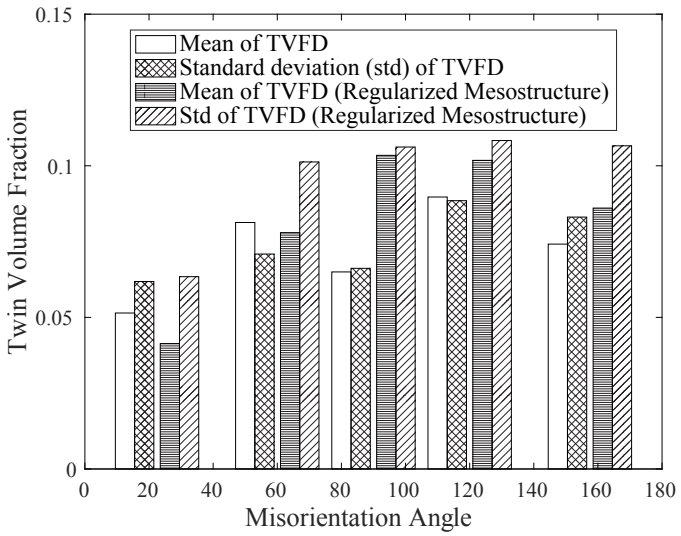

Figure 11: Maximum twin concentration discrepancy and misorientation in mesostructures with (a) randomized polygonal particle geometries and (b) regularized particle geometries. Mean and standard deviation are computed in five intervals ((0°,45°), (45°,75°), (75°,105°), (105°,135°) and (135°,180°)).

Stress distributions of these four cases are plotted in Fig. 12. The stress contours are at time instances, where the wave front is approximately in the middle of the mesostructure. With increasing impact velocity, the response transitions from elastop-lastic wave propagation (Fig. 12a) to near hydrodynamic shock propagation (Fig. 12d). A clear separation of the shock wave is observed in the latter three simulations, while the 100 m/s case shows continuous compression trailing the wave front. Even at the highest impact velocity, stress distribution at the shock front is highly heterogeneous indicating the role of morphology on the dynamic response.

The corresponding twin volume fraction contours are shown in Fig. 13. The regions of the mesostructure with elevated twin concentration are not significantly affected by the impact loading amplitude. Naturally, those grains, where the twin system is favorably aligned with the orientation of shock propagation exhibit significant twin volume fractions. For low to moderate impact velocities (i.e., 100-300 m/s), the sites of localized peak volume concentration occur at the triple junctions near the surface of the volume. Under the high impact velocity condition, the location of the peak volume fraction occurs at the interior of the grain near the impact surface in mesostructure as shown in Fig. 13d. Figure 14 shows the relationship between the peak twin volume fraction and the applied impact velocity. At the range of loading tested in this study, a clear linear trend exists with very substantial twin concentrations (90%) at high impact velocity. Considering localized twinning concentrations as potential hot-spots in the mesostructure, the simulations indicate that triple junctions could be of significance in detonation initiation.

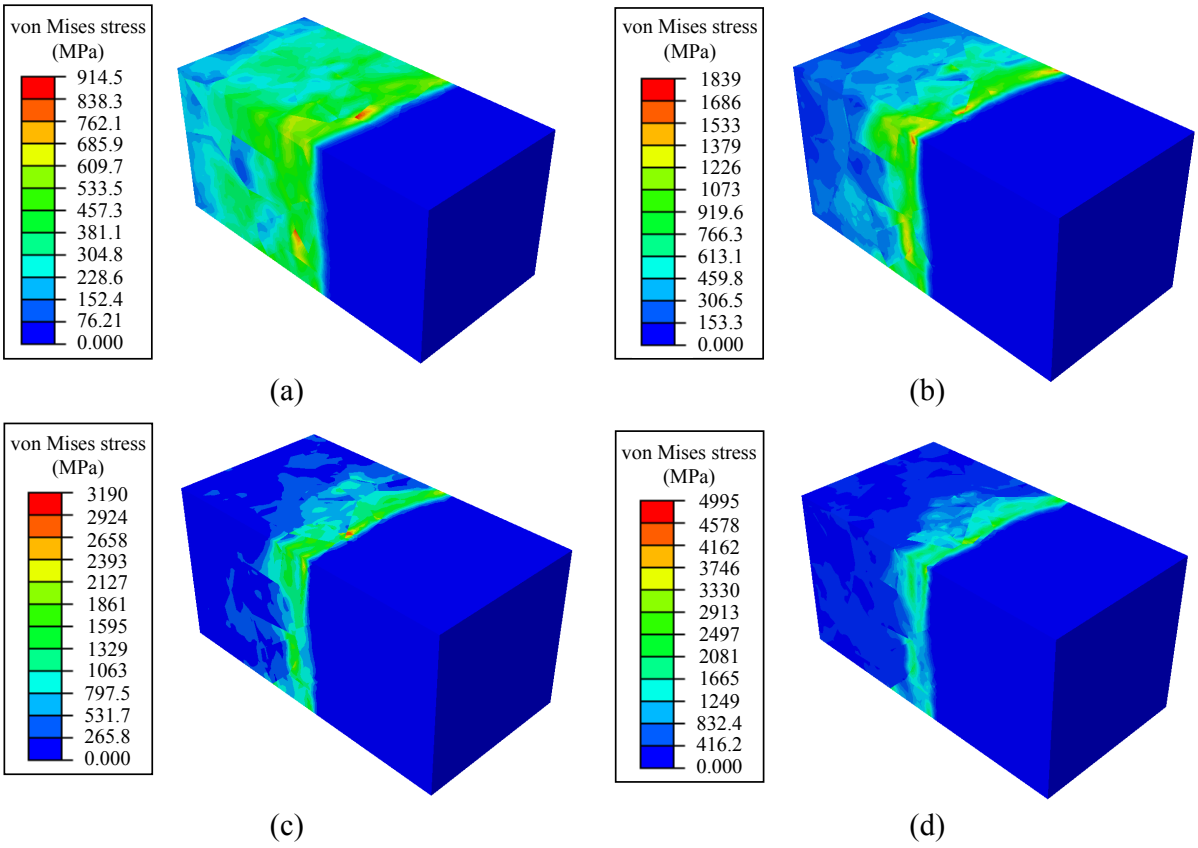

Figure 12: Stress contour of mesoscale structure subjected to impact loading (a) 100 m/s at t=0.12 μs, (b) 200 m/s at t=0.10 μs, (c) 300 m/s at t=0.098 μs and (d) 400 m/s at t=0.095 μs.

5 Conclusion

This manuscript presented the investigations of mechanical twinning behavior of crystalline β-HMX with respect to crystal orientation, mesoscale structure and loading amplitude under given shock/sub-shock impact through a CPFE framework with large volumetric deformation. This manuscript serves as a starting point of modeling mechanical twinning from a physics-based perspective, and it can be further improved with additional experimental data about twinning and detwinning. The results show that the deformation twinning has strong orientation dependency in single crystal and in polycrystal configurations. Compared with the more realistic mesostructure, the regularized structure generates lower peak twin volume fraction due to the reduction of sharp corners of particles. Twinning phenomenon becomes more evident at higher strain rate which further highlights the importance of modeling twinning through a physically meaningful fashion. Once more information, particularly information from lower scales, become available through experimental observation or first principle calculations, the proposed model can be improved with more accurate calibration and additional physics can be incorporated to capture material behavior at mesoscale.

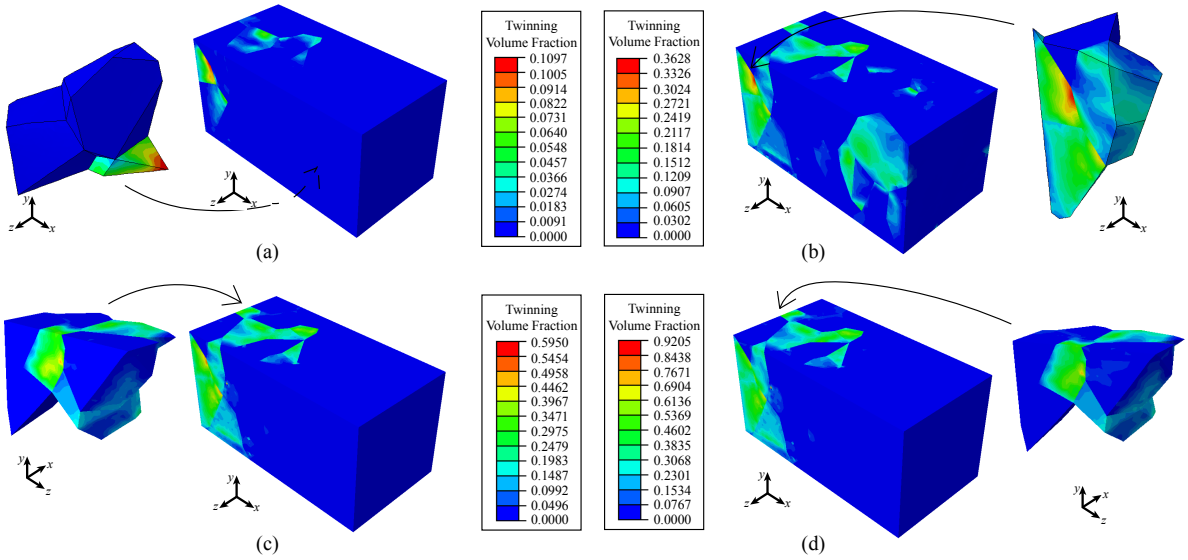

Figure 13: Twin volume fraction contour of mesoscale structure subjected to impact loading (a) 100 m/s at t=0.25 μs, (b) 200 m/s at t=0.125 μs, (c) 300 m/s at t=0.098 μs and (d) 400 m/s at t=0.095 μs.

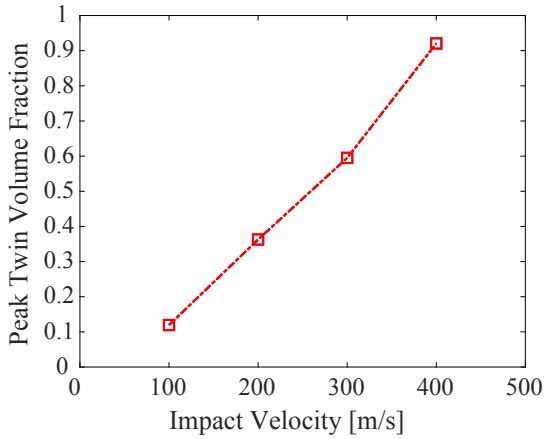

Figure 14: Rate-dependent twin formation in the HMX polycrystal.

Acknowledgments

The authors gratefully acknowledge the financial support from the Air Force Office of Scientific Research, Dynamic Materials and Interactions Program (Grant No.: FA9550- 15-1-0202, Program Manager: Dr. Martin Schmidt).

References

[1] R. W. Armstrong. Dislocation mechanics aspects of energetic material composites. *Rev. Adv. Mater. Sci*, 19:13–40, 2009.

[2] R. W. Armstrong, H. L. Ammon, Z. Y. Du, W. L. Elban, and X. J. Zhang. Energetic crystal-lattice-dependent responses. *MRS Online Proceedings Library Archive*, 296, 1992.

[3] J. R. Asay, G. R. Fowles, G. E. Durall, M. H. Miles, and R. F. Tinder. Effects of point defects on elastic precursor decay in lif. *Journal of Applied Physics*, 43(5):2132–2145, 1972.

[4] R. A. Austin and D. L. McDowell. A dislocation-based constitutive model for viscoplastic deformation of fcc metals at very high strain rates. *International Journal of Plasticity*, 27(1):1–24, 2011.

[5] R. A. Austin, N. R. Barton, J. E. Reaugh, and L. E. Fried. Direct numerical simulation of shear localization and decomposition reactions in shock-loaded hmx crystal. *Journal of Applied Physics*, 117(18):185902, 2015.

[6] N. R. Barton, J. Knap, A. Arsenlis, R. Becker, R. D. Hornung, and D. R. Jefferson. Embedded polycrystal plasticity and adaptive sampling. *International Journal of Plasticity*, 24(2):242–266, 2008.

[7] N. R. Barton, N. W. Winter, and J. E. Reaugh. Defect evolution and pore collapse in crystalline energetic materials. *Modelling and Simulation in Materials Science and Engineering*, 17(3):035003, 2009.

[8] R. Becker. Effects of crystal plasticity on materials loaded at high pressures and strain rates. *International Journal of Plasticity*, 20(11):1983–2006, 2004.

[9] R. R. Bernecker. Observations on the hugoniot for hmx. *In AIP Conference Proceedings*, 370(1):141–144, 1996.

[10] M. Bevis and A. G. Crocker. Twinning modes in lattices. *Proceedings of the Royal Society of London. A. Mathematical and Physical Sciences*, 313(1515):509–529, 1969.

[11] F. Birch. Finite elastic strain of cubic crystals. *Physical review*, 71(11):809, 1947.

[12] H. H. Cady. Growth and defects of explosives crystals. *MRS Online Proceedings Library Archive*, 296:243–254, 1992.

[13] C. S. Choi and H. P. Boutin. A study of the crystal structure of β-cyclotetramethylene tetranitramine by neutron diffraction. *Acta Crystallographica Section B: Structural Crystallography and Crystal Chemistry*, 26(9):1235–1240, 1970.

[14] J. W. Christian and S. Mahajan. Deformation twinning. *Progress in materials science*, 39(1-2):1–157, 1995.

[15] R. J. Clifton and X. Markenscoff. Elastic precursor decay and radiation from nonuniformly moving dislocations. *Journal of the Mechanics and Physics of Solids*, 29(3):227–251, 1981.

[16] M. W. Conroy, I. I. Oleynik, S. V. Zybin, and C. T. White. First-principles anisotropic constitutive relationships in β-cyclotetramethylene tetranitramine (β-hmx). *Journal of Applied Physics*, 104(5):053506, 2008.

[17] L. Davison. *Fundamentals of shock wave propagation in solids*. Springer Science & Business Media, 2008.

[18] C. Deng, X. Xue, Y. Chi, H. Li, X. Long, and C. Zhang. Nature of the enhanced self-heating ability of imperfect energetic crystals relative to perfect ones. *The Journal of Physical Chemistry C*, 121(22):12101–12109, 2017.

[19] J. R. Deschamps, M. Frisch, and D. Parrish. Thermal expansion of hmx. *Journal of Chemical Crystallography*, 41(7):966–970, 2011.

[20] J. J. Dick, D. E. Hooks, and R. Menikoff. Elastic–plastic wave profiles in cyclotetramethylene tetranitramine crystals. *Journal of Applied Physics*, 96(1):374–379, 2004.

[21] J. E. Field. Hot spot ignition mechanisms for explosives. *Accounts of chemical Research*, 25(11):489–496, 1992.

[22] P. S. Follansbee and U. F. Kocks. A constitutive description of the deformation of copper based on the use of the mechanical threshold stress as an internal state variable. *Acta Metallurgica*, 36(1):81–93, 1988.

[23] H. G. Gallagher, J. C. Miller, D. B. Sheen, J. N. Sherwood, and R. M. Vrcelj. Mechanical properties of β-hmx. *Chemistry Central Journal*, 9(1):22, 2015.

[24] Y. F. Gao and Z. Suo. The orientation of the self-assembled monolayer stripes on a crystalline substrate. *Journal of the Mechanics and Physics of Solids*, 51(1):147–167, 2003.

[25] N. Grilli and M. Koslowski. The effect of crystal orientation on shock loading of single crystal energetic materials. *Computational Materials Science*, 155:235–245, 2018.

[26] J. C. Gump and S. M. Peiris. Isothermal equations of state of β octahydro-1, 3, 5, 7-tetranitro-1, 3, 5, 7-tetrazocine at high temperatures. *Journal of applied physics*, 97(5): 053513, 2005.

[27] M. E. Gurtin and K. Spear. On the relationship between the logarithmic strain rate and the stretching tensor. *International Journal of Solids and Structures*, 19(5):437–444, 1983.

[28] D. B. Hardin, J. J. Rimoli, and M. Zhou. Analysis of thermomechanical response of polycrystalline hmx under impact loading through mesoscale simulations. *AIP Advances*, 4(9):097136, 2014.

[29] M. Herrmann, W. Engel, and N. Eisenreich. Thermal expansion, transitions, sensitivities and burning rates of hmx. *Propellants, Explosives, Pyrotechnics*, 17(4):190–195, 1992.

[30] A. Hoger. The stress conjugate to logarithmic strain. *International Journal of Solids and Structures*, 23(12):1645–1656, 1987.

[31] D. E. Hooks, D. B. Hayes, D. E. Hare, D. B. Reisman, K. S. Vandersall, J. W. Forbes, and C. A. Hall. Isentropic compression of cyclotetramethylene tetranitramine (hmx) single crystals to 50 gpa. *Journal of applied physics*, 99(12):124901, 2006.

[32] R. Hu, C. Prakash, V. Tomar, M. Harr, and I. E. Gunduzand C. Oskay. Experimentally-validated mesoscale modeling of the coupled mechanical–thermal response of ap–htpb energetic material under dynamic loading. *International Journal of Fracture*, 203(1-2): 277–298, 2017.

[33] A. Jain and S. R. Agnew. Modeling the temperature dependent effect of twinning on the behavior of magnesium alloy az31b sheet. *Materials Science and Engineering: A*, 462 (1-2):29–36, 2007.

[34] N. Jia, F. Roters, P. Eisenlohr, C. Kords, and D. Raabe. Non-crystallographic shear banding in crystal plasticity fem simulations: Example of texture evolution in α-brass. *Acta Materialia*, 60(3):1099–1115, 2012.

[35] J. N. Johnson and W. Band. Investigation of precursor decay in iron by the artificial viscosity method. *Journal of Applied Physics*, 38(4):1578–1585, 1967.

[36] S. R. Kalidindi. Incorporation of deformation twinning in crystal plasticity models. *Journal of the Mechanics and Physics of Solids*, 46(2):267–290, 1998.

[37] S. R. Kalidindi. Modeling anisotropic strain hardening and deformation textures in low stacking fault energy fcc metals. *International Journal of Plasticity*, 17(6):837–860, 2001.

[38] S. W. Key. Grüneisen tensor for anisotropic materials. *Journal of Applied Physics*, 38(7): 2923–2928, 1967.

[39] M. Khan, A. Pal, and C. R. Picu. Dislocation mobility and critical stresses at finite temperatures in molecular crystal cyclotetramethylene tetranitramine (β-hmx). *Modelling and Simulation in Materials Science and Engineering*, 26(8):085009, 2018.

[40] M. V. Klassen-Neklyudova. *Mechanical twinning of crystals*. Springer Science & Business Media, 2012.

[41] U. F. Kocks, A. AS, and A. MF. Thermodynamics and kinetics of slip. 1975.

[42] B Kratochvíl. Anthony kelly a kevin m. knowles: Crystallography and crystal defects. *Chemické listy*, 107(5):400–400, 2013.

[43] A. C. Landerville, M. W. Conroy, M. M. Budzevich, Y. Lin, C. T. White, and I. I. Oleynik. Equations of state for energetic materials from density functional theory with van der waals, thermal, and zero-point energy corrections. *Applied Physics Letters*, 97 (25):251908, 2010.

[44] H. Li, R. Xu, B. Kang, J. Li, X. Zhou, C. Zhang, and F. Nie. Influence of crystal characteristics on the shock sensitivities of cyclotrimethylene trinitramine, cyclotetramethylene tetranitramine, and 2, 4, 6, 8, 10, 12-hexanitro-2, 4, 6, 8, 10, 12-hexaazatetra-cyclo [5, 5, 0, 03, 1105, 9] dodecane immersed in liquid. *Journal of Applied Physics*, 113(20):203519, 2013.

[45] D. H. Liebenberg, R. W. Armstrong, and J. J. Gilman. Structure and properties of energetic materials. Technical report, Materials Research Society Pittsburgh PA, 1992.

[46] S. Mahajan and G. Y. Chin. Formation of deformation twins in fcc crystals. *Acta metallurgica*, 21(10):1353–1363, 1973.

[47] S. P. Marsh. *LASL shock Hugoniot data*, volume 5. Univ of California Press, 1980.

[48] N. Mathew and R. C. Picu. Slip asymmetry in the molecular crystal cyclotrimethylenetrinitramine. *Chemical Physics Letters*, 582:78–81, 2013.

[49] N. Mathew and T. Sewell. Pressure-dependent elastic coefficients of β-hmx from molecular simulations. *Propellants, Explosives, Pyrotechnics*, 43(3):223–227, 2018.

[50] R. Menikoff and T. D. Sewell. Fitting forms for isothermal data. *International Journal of High Pressure Research*, 21(2):121–138, 2001.

[51] R. Menikoff, J. J. Dick, and D. E.Hooks. Analysis of wave profiles for single-crystal cyclotetramethylene tetranitramine. *Journal of Applied Physics*, 97(2):023529, 2005.

[52] M. A. Meyers, O. Vöhringer, and V. A. Lubarda. The onset of twinning in metals: a constitutive description. *Acta materialia*, 49(19):4025–4039, 2001.

[53] B. Olinger, B. Roof, and H. Cady. The linear and volume compression of β-hmx and rdx. In *Actes du Symposium International sur le Comportement des Milieux Denses Sous Hautes Pressions Dynamiques*, pages 3–8. Commissariat a l'Energie Atomique Paris, 1978.

[54] A. Pal and C. R. Picu. Peierls–nabarro stresses of dislocations in monoclinic cyclotetramethylene tetranitramine (β-hmx). *Modelling and Simulation in Materials Science and Engineering*, 26(4):045005, 2018.

[55] A. Pal and C. R. Picu. Non-schmid effect of pressure on plastic deformation in molecular crystal hmx. *Journal of Applied Physics*, 125(21):215111, 2019.

[56] S. J. P. Palmer and J. E. Field. The deformation and fracture of β-hmx. *Proceedings of the Royal Society of London. Series A: Mathematical, Physical and Engineering Sciences*, 383(1785):399–407, 1982.

[57] Y. Partom. Elastic precursor decay calculation. *Journal of applied physics*, 59(8):2716–2727, 1986.

[58] Q. Peng, G. Wang, G. R. Liu, and S. De. Structures, mechanical properties, equations of state, and electronic properties of β-hmx under hydrostatic pressures: a dft-d2 study. *Physical Chemistry Chemical Physics*, 16(37):19972–19983, 2014.

[59] C. Prakash, I. E. Gunduz, C. Oskay, and V. Tomar. Effect of interface chemistry and strain rate on particle-matrix delamination in an energetic material. *Engineering Fracture Mechanics*, 191:46–64, 2018.

[60] G. Proust, C. N. Tomé, and G. C. Kaschner. Modeling texture, twinning and hardening evolution during deformation of hexagonal materials. *Acta Materialia*, 55(6):2137–2148, 2007.

[61] G. Proust, C. N. Tomé, A. Jain, and S. R. Agnew. Modeling the effect of twinning and detwinning during strain-path changes of magnesium alloy az31. *International Journal of Plasticity*, 25(5):861–880, 2009.

[62] R. Quey, P. R. Dawson, and F. Barbe. Large-scale 3d random polycrystals for the finite element method: Generation, meshing and remeshing. *Computer Methods in Applied Mechanics and Engineering*, 200(17-20):1729–1745, 2011.

[63] P. J. Rae, H. T. Goldrein, S. J. P. Palmer, J. E. Field, and A. L. Lewis. Quasi–static studies of the deformation and failure of β–hmx based polymer bonded explosives. *Proceedings of the Royal Society of London. Series A: Mathematical, Physical and Engineering Sciences*, 458(2019):743–762, 2002.

[64] F. Roters, P. Eisenlohr, L. Hantcherli, D. D. Tjahjanto, T. R. Bieler, and D. Raabe. Overview of constitutive laws, kinematics, homogenization and multiscale methods in crystal plasticity finite-element modeling: Theory, experiments, applications. *Acta Materialia*, 58(4):1152–1211, 2010.

[65] K. W. Schuler and J. W. Nunziato. The dynamic mechanical behavior of polymethyl methacrylate. *Rheologica Acta*, 13(2):265–273, 1974.

[66] T. D. Sewell, R. Menikoff, D. Bedrov, and G. D. Smith. A molecular dynamics simulation study of elastic properties of hmx. *The Journal of Chemical Physics*, 119(14):7417–7426, 2003.

[67] D. B. Sheen, J. N. Sherwood, H. G. Gallagher, A. Littlejohn, and A. Pearson. Final report to the us office of naval research-an investigation of mechanically induced lattice defects in energetic materials. 1993.

[68] C. B. Skidmore, D. S. Phillips, S. F. Son, and B. W. Asay. Characterization of hmx particles in pbx 9501. In *AIP Conference Proceedings*, volume 429, pages 579–582. AIP, 1998.

[69] D. C. Sorescu, B. M. Rice, and D. L. Thompson. Theoretical studies of the hydrostatic compression of rdx, hmx, hniw, and petn crystals. *The Journal of Physical Chemistry B*, 103(32):6783–6790, 1999.

[70] J. W. Taylor. Dislocation dynamics and dynamic yielding. *Journal of Applied Physics*, 36(10):3146–3150, 1965.

[71] C. N. Tomé, P. J. Maudlin, R. A. Lebensohn, and G. C. Kaschner. Mechanical response of zirconium—i. derivation of a polycrystal constitutive law and finite element analysis. *Acta Materialia*, 49(15):3085–3096, 2001.

[72] J. VonNeumann and R. D. Richtmyer. A method for the numerical calculation of hydrodynamic shocks. *Journal of applied physics*, 21(3):232–237, 1950.

[73] S. M. Walley, J. E. Field, and M. W. Greenaway. Crystal sensitivities of energetic materials. *Materials Science and Technology*, 22(4):402–413, 2006.

[74] H. Wang, P. D. Wu, J. Wang, and C.N. Tomé. A crystal plasticity model for hexagonal close packed (hcp) crystals including twinning and de-twinning mechanisms. *International Journal of Plasticity*, 49:36–52, 2013.

[75] X. Wang, Y. Wu, and F. L. Huang. Thermal–mechanical–chemical responses of polymer-bonded explosives using a mesoscopic reactive model under impact loading. *Journal of hazardous materials*, 321:256–267, 2017.

[76] Y. Wen, X. Xue, X. Zhou, F. Guo, X. Long, Y. Zhou, H. Li, and C. Zhang. Twin induced sensitivity enhancement of hmx versus shock: a molecular reactive force field simulation. *The Journal of Physical Chemistry C*, 117(46):24368–24374, 2013.

[77] B. W. White and C. M. Tarver. Ignition and growth modeling of detonation reaction zone experiments on single crystals of petn and hmx. *In AIP Conference Proceedings*, 1793(1): 030001, 2017.

[78] R. E. Winter and J. E. Field. The role of localized plastic flow in the impact initiation of explosives. *Proceedings of the Royal Society of London A: Mathematical, Physical and Engineering Sciences*, 343(1634):399–413, 1975.

[79] C.S. Yoo and H. Cynn. Equation of state, phase transition, decomposition of β-hmx (octahydro-1, 3, 5, 7-tetranitro-1, 3, 5, 7-tetrazocine) at high pressures. *The Journal of Chemical Physics*, 111(22):10229–10235, 1999.

[80] A. R. Zamiri and S. De. Deformation distribution maps of β-hmx molecular crystals. *Journal of Physics D: Applied Physics*, 43(3):035404, 2010.

[81] A. R. Zamiri and S. De. Modeling the anisotropic deformation response of β-hmx molecular crystals. *Propellants, Explosives, Pyrotechnics*, 36(3):247–251, 2011.

[82] J. M. Zaug, M. R. Armstrong, J. C. Crowhurst, L. Feranti, R. Swan, R. Gross, N. E. Teshlich, M. Wall, R. A. Austin, and L. E. Fried. Ultrafast dynamic response of single crystal petn and β-hmx (no. llnl-conf-656341). Technical report, 2014.

[83] M. Zecevic, F. L. Addessio, M. J. Cawkwell, K. J. Ramos, and D. J. Luscher. Single crystal plasticity model with deformation twinning for the high rate deformation of β-hmx. In *AIP Conference Proceedings*, volume 2272, page 070058. AIP Publishing LLC, 2020.

[84] X. Zhang and C. Oskay. Material and morphology parameter sensitivity analysis in particulate composite materials. *Computational Mechanics*, 62(3):543–561, 2017.

[85] X. Zhang and C. Oskay. Plastic dissipation sensitivity to mechanical properties in polycrystalline β-hmx subjected to impact loading. *Mechanics of Materials*, 138:103079, 2019.

[86] T. Zhou, S. V. Zybin, Y. Liu, F. Huang, and W. A. Goddard III. Anisotropic shock sensitivity for β-octahydro-1, 3, 5, 7-tetranitro-1, 3, 5, 7-tetrazocine energetic material under compressive-shear loading from reaxff-lg reactive dynamics simulations. *Journal of Applied Physics*, 111(12):124904, 2012.